crystals

MDPI

Article

Gemological and Chemical Characterization of Gem-Quality Titanite from Morocco

Yu Yuan [1], Zhuang Miao [1,*], Yi Zhao [1,*], Bo Xu [1,2], Jialu Gu [1] and Pengyu Yuan [1]

[1] Frontiers Science Center for Deep-Time Digital Earth and State Key Laboratory of Geological Processes and Mineral Resources, School of Gemology, China University of Geosciences, Beijing 100083, China; 2009220025@email.cugb.edu.cn (Y.Y.); bo.xu@cugb.edu.cn (B.X.); 3001210024@email.cugb.edu.cn (J.G.); 3009230004@email.cugb.edu.cn (P.Y.)

[2] Beijing SHRIMP Center, Chinese Academy of Geological Sciences, Beijing 100037, China

* Correspondence: zhuangmiao@cugb.edu.cn (Z.M.); zhaoyi0102@cugb.edu.cn (Y.Z.)

Abstract: Titanite is a widespread accessory mineral in igneous, metamorphic, and hydrothermal rocks, but few comply with gem-grade requirements. Previous studies on Moroccan titanite focused on elementary composition and U-Pb dating. In this study, two gem-grade titanites (MA-1 and MA-2) from the Moroccan Central High Atlas were investigated through gemological and chemical studies, including infrared spectrum, Raman spectrum, SEM-EDS, and LA-ICP-MS. Two titanite samples are yellow, transparent–translucent with a greasy luster, 3.5 and 2.5 mm long. MA-1 and MA-2 have similar gemological properties, the refractive index (RI) is beyond the range of the refractometer (>1.78), the specific gravity (SG) values fall in the range of 3.52~3.54 and both are inert to short-wave and long-wave UV radiation. The spectral characteristics have high consistency with the RRUFF database. The major elements' composition shows a negative correlation between Al, Fe, V, and Ti, suggesting the titanites underwent substitutions such as (Al, Fe^{3+}) + (F, OH) ↔ Ti + O. The titanite samples, characterized by a low abundance of REE (802~4088 ppm) and enriched in LREE, exhibit positive Eu (δEu: 1.53~7.79) and Ce (δCe: 1.08~1.33) anomalies, indicating their formation in a hydrothermal environment with low oxygen fugacity. The $^{238}U/^{206}Pb$ and $^{207}Pb/^{206}Pb$ ratios of the titanites yield lower intercept ages of 152.6 ± 2.2 and 151.4 ± 5.3 Ma (1s), consistent with their weighted average $^{206}Pb/^{238}U$ ages of 152.3 ± 2.0 and 150.7 ± 3.2 Ma (1s) respectively. The results of U-Pb dating are matched with the second main magmatic activities in the High Atlas intracontinental belt of Morocco during the Mesozoic to Cenozoic period. Moreover, the two titanite samples have almost no radiational damage. All the results show that the titanite from High Atlas, Morocco, has the potential to be a reference material for LA-ICP-MS U–Pb dating, but further experiments are needed to be sure.

Keywords: titanite; infrared spectroscopy; Raman spectroscopy; LA-ICP-MS; Morocco

Citation: Yuan, Y.; Miao, Z.; Zhao, Y.; Xu, B.; Gu, J.; Yuan, P. Gemological and Chemical Characterization of Gem-Quality Titanite from Morocco. *Crystals* **2024**, *14*, 80. https://doi.org/10.3390/cryst14010080

Academic Editor: Sergey V. Krivovichev

Received: 24 November 2023
Revised: 7 January 2024
Accepted: 9 January 2024
Published: 14 January 2024

1. Introduction

Titanite ($CaTiSiO_5$) is commonly found as an accessory mineral in igneous, metamorphic, and hydrothermal rocks [1–4]. Despite the low hardness of titanite (Mohs hardness is 5), the diverse colors and brilliant hues exhibited by titanite contribute to its attractiveness as a gemstone. Gem-quality titanite is primarily sourced in Russia, China, Morocco, Sri Lanka, Pakistan, Madagascar, Brazil, and other places (Figure 1) [5–7]. However, there is a gap in the study of the gemological and mineralogical characteristics of gem-grade titanite and a lack of a comparative analysis of titanites from different producing areas.

Natural titanite is di-cationic nesosilicate with a space group $P2_1/a$. The $[SiO_4]^{4-}$ tetrahedra are surrounded by the $[CaO_7]^{12-}$ and $[TiO_6]^{8-}$ groups, which form chains parallel to the 'a' axis. The $[TiO_6]^{8-}$ octahedra exhibit non-central positions of the Ti^{4-} ions. Each $[CaO_7]^{12-}$ polyhedron links one edge to one $[SiO_4]^{4-}$ tetrahedron, four edges

to $[TiO_6]^{8-}$ groups, and two edges to other $[CaO_7]^{12-}$ groups. O^{2-} can be replaced by F^- and OH^- [8,9].

Figure 1. Global gem-grade titanite-producing locations (hued portions) map. The red dot represents the locations of the Moroccan titanite samples.

Titanite is distinguished by the abundance of rare earth elements (REEs) and high field strength elements (HFSEs) [10–12], which serve as important indicators of its formation conditions [1,13]. Titanite contains considerable amounts of U (10 to >100 ppm) in the crystalline structure, making it an effective mineral for U–Pb dating [2,13,14]. In recent years, laser ablation inductively coupled plasma mass spectrometry (LA-ICP-MS) has emerged as an efficient technique for microanalysis of U–Pb dating and trace elements [3,11,15]. The existing titanite reference materials are no longer sufficient for geochronology analysis, which hinders its broader application [16–18].

In this study, the gemological and mineralogical characteristics of Moroccan titanites were comparatively investigated by the new data from conventional gemology, spectroscopy, and chemical composition. We aim to (1) enrich the gemological and mineralogical studies on titanite; (2) explore the formation conditions and sources of the titanites, providing important indications for the titanite origin; (3) investigate the potential of the studied titanites as reference materials for U–Pb dating by LA-ICP-MS.

2. Geological Setting

Morocco is located northwest of Africa, which is affected by the West African Craton, the Atlantic Ocean, and the Alpine orogenic belt. Influenced and controlled by multiple tectonic activities since the Precambrian, several tectonic units such as the Rif belt, High-Atlas, Anti-Atlas, and Meseta were formed in Morocco. The gem-grade titanite of Morocco studied in this paper was produced in the central region of the High Atlas (CHA, Figure 2A).

The High Atlas region constitutes an intracontinental Alpine orogen, resulting from the convergence of the African and Eurasian plates. Its formation began in the early Mesozoic era due to the reactivation of an ancient fault in Pangea [19–22]. This orogenic belt consists of various segments, with the Central High Atlas being the deepest part (Figure 2B) [22–24]. Intracontinental rifts were formed in the High Atlas and Middle Atlas during the Triassic to Cretaceous period, accompanied by volcanic activity in the lower Jurassic era [25]. These Mesozoic rifts underwent inversion during the Cenozoic era, leading to sediment deposition in adjacent foreland basins [26,27].

The Central High Atlas primarily comprises limestone and continental red rock formations from the Mid-Jurassic period. These formations were active during Jurassic–Cretaceous orogeny, folding, and magmatism activity [28]. The anticlinal ridges at its core were formed through significant alkaline to transitional magmatism between approx-

imately 165 Ma and 125 Ma during this time [28–30]. Magma can be found intruding along faults and narrow anticlinal ridges or intercalated within thick Mesozoic sedimentary layers [28,31,32]. Notably, gem deposits such as Tasraft (Ta), Anemzi (Az), Tassent (Ts), Ait Daoud-Toumliline (AD), and Tirrhist-Inouzane (Tr-In) in the Central High Atlas, always exhibit spatial associations with the Jurassic–Cretaceous alkaline intrusions. In this study, titanite samples were collected from the Tasraft (Ta) deposit.

The Tasraft (Ta) deposit exhibits an anticlinal structure. Wide Middle Jurassic-cored synclines are separated by narrow Early Jurassic-cored anticlines where the mafic–felsic intrusions outcrop (Figure 2C). The magmatic ridges form elongated layered intrusions generally delimited by tectonic contacts with the country rocks. The tectonic contacts are mostly vertical faults marked by breccia. The intrusions exhibit pervasive faulting and a lack of contact metamorphic aureoles. The faults fragmented each intrusion into several blocks, partially hiding primary relationships [24,31].

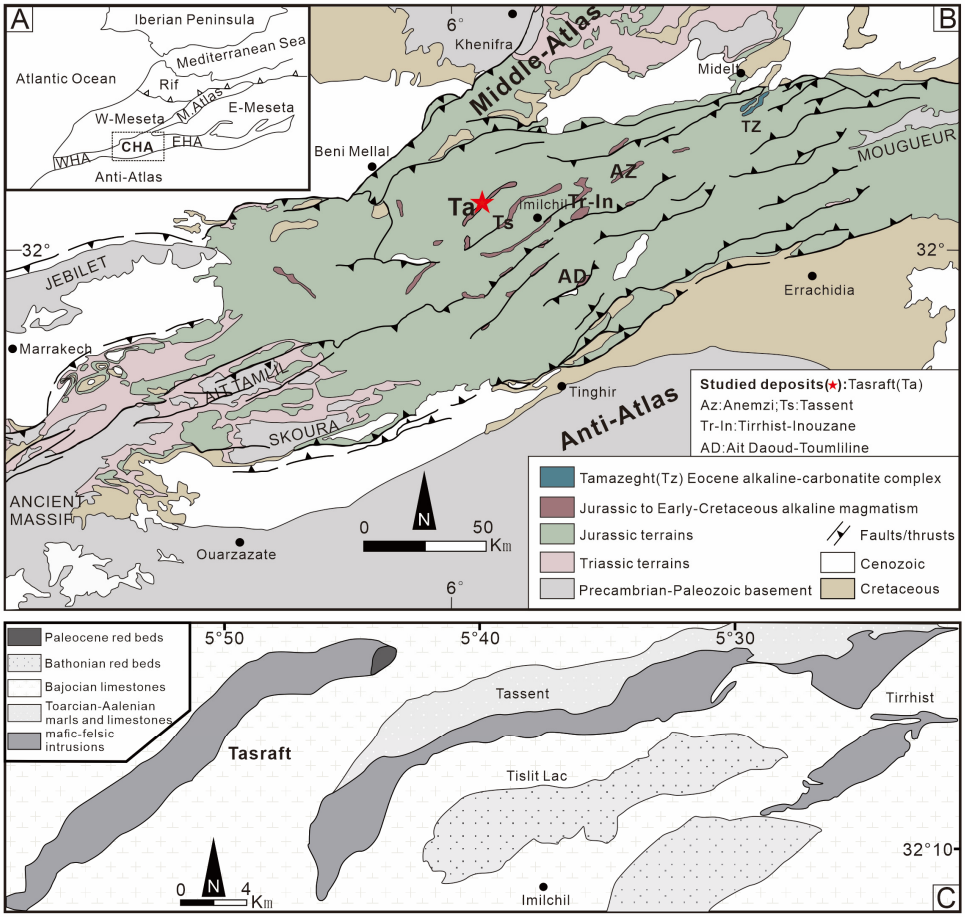

Figure 2. (**A**) Map of the Central High Atlas (CHA) region in north Morocco. (**B**) Geology map of the Central High Atlas (modified from [24]), with the location of samples marked with a red star. (**C**) Geological map of the Tasraft and Tassent anticlinal ridges in the Imilchil area (modified from [31]).

3. Materials and Methods

3.1. Sample Description

In this study, a piece of rock with some yellow euhedral–subhedral titanites up to 3.5 mm in size (Figure 3A) was collected from the Tasraft (Ta) deposit in the Central High Atlas, Morocco, whose GPS coordinate is 32°10′42.15″ N, 5°52′58.92″ W [24]. From all the samples, we chose the two monocrystal titanites (MA-1, MA-2) for testing. MA-1 is a yellow tabular crystal 3.5 mm long, transparent with a greasy luster (Figure 3B). The

surface of MA-1 is smooth without damage. MA-2 is a yellow prismatic crystal 2.5 mm long, shorter than MA-1, and it is translucent with a weak greasy luster (Figure 3C). MA-2 has middle degrees of surface damage. The two raw titanites have some natural facets for gemological and spectroscopic investigation. Specific gravity (SG), refractive indices (RIs), and fluorescence reactions were measured by standard gemological instruments.

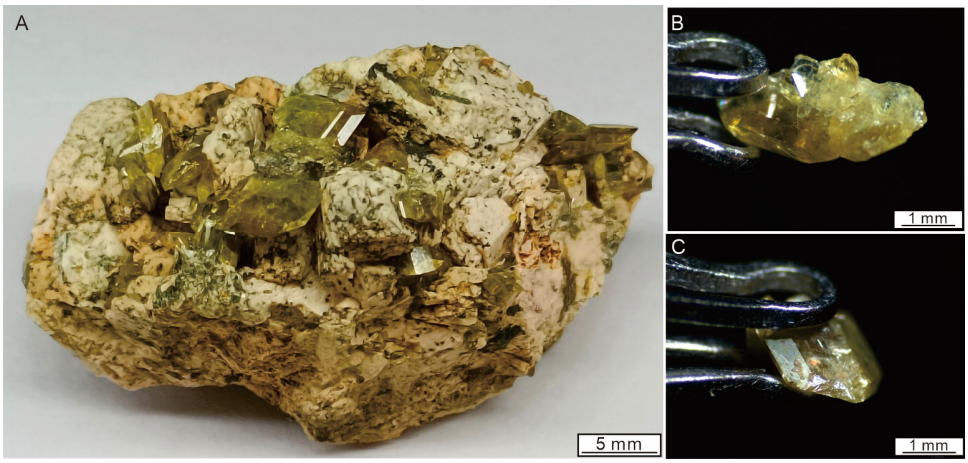

Figure 3. The photos of titanite samples were collected and examined in this study. (**A**) Rough titanite with surrounding rock; (**B**) MA-1; (**C**) MA-2.

3.2. Gemological Observation and Spectroscopy Analysis

The two titanite samples were analyzed at the Gemological Experimental Teaching Center of the School of Gemology, China University of Geosciences (Beijing) to obtain their properties of gemology and spectroscopy.

The refractive index (RI) of the titanite samples was measured using a refractometer from Xueyuan Jewelry Technologies in Wuhan, China. Diiodomethane was utilized as the medium for determining the refractive index. The Nanjing Baoguang GI-MP22 binocular gemological microscope was utilized to observe the internal characteristics and photomicrographs, employing magnifications of 10× and 40×. The specific gravity (SG) of the sample was measured using the hydrostatic weighing method. The Chelsea color filter (CCF) from Baoguang Technologies in Nanjing, China, was used to observe the samples. The fluorescence of the samples was observed using ultraviolet light with primary wavelengths of 365 nm and 254 nm.

The infrared spectra were collected by the transmission method of the KBr pellet pressed-disk technique, using a Tensor 27 Fourier Transform Infrared Spectrometer from Bruker in Germany. The transmission method conditions were as follows: a resolution of 4 cm^{-1}, grating size of 6 mm, test range between 400 and 4000 cm^{-1}, sample scanning time of 128 scans, and background scanning time of 128 scans. The results are presented in absorbance. Samples for FTIR analysis were prepared by mixing dried samples with KBr and compression into disks. Before the test, 150 mg KBr was ground into 200 mesh powder and compressed into a disk, which was measured by the transmission method as a background reference spectrum.

The Raman spectra were collected using an HR-Evolution micro laser Raman spectrometer manufactured by HORIBA in France, at 532 nm with a ×50_VIS objective and unpolarized laser source. The experiment conditions were as follows: scanning range from 400 to 1200 cm^{-1}, slit width adjusted to be 100 μm, and grating size selected as 600 gr/mm. The laser power was rated at 100 mW, and the ND filter was 25%. The scanning time was set at 4s. The number of accumulations was 3. The Raman spectra were obtained from each crystal face parallel to the b-axis.

3.3. SEM Analysis

Two titanite samples were first mechanically crushed, after which the pure parts of the samples were placed in an epoxy block to polish them to the largest surface. The polished portions were surface carbon blasted before testing. The TESCAN field emission scanning electron microscope (MIRA 3LMH) was used to capture backscattered electron (BSE) images at China University of Geosciences (Beijing), with the following settings: acceleration voltage of 7 kV, absorption current of 1.2 nA, scan time of 80 s.

3.4. Chemical Analysis

3.4.1. Major Elements

The major elements of titanite samples were collected on a CARLZEISS MERLIN Compact scanning electron microscope (SEM, manufactured in Ostalbkreis, Baden-Wurttemberg, Germany by Carl Zeiss AG) with an OXFORD IE250 energy disperse spectroscopy (EDS, manufactured in Abingdon, Oxfordshire, UK by OXFORD INSTRUMENTS) system at the Beijing Shrimp Center. Samples were covered with Au to avoid the charge accumulation effect. SEM-EDS analyses were performed under the following conditions: electron beam current = 10 nA, constant acceleration voltage = 20 kV, working distance = 8.8 mm, aperture size = 60 μm, and analysis time = 40 s for each analysis. The EDS analysis used the standard ZAF corrections (Z = atomic number, A = atomic absorption, F = X-ray fluorescence), which are already installed with the software and make corrections between the peak and background of the element. The chemical elements analyzed were O, F, Na, Mg, Al, Si, K, Ca, Ti, V, Cr, Mn, Fe, and Zr for a total of 66 analyses situated on both the borders and center of the fragments. The Aztec software was used to process data, which enables the deduction of the background value and distinguishes overlapping peaks through deconvolution processing, facilitating the automatic separation of spectral peaks. All data were normalized and the unit formula was calculated based on 5 oxygen atoms.

3.4.2. Trace Elements and U-Pb Dating

For trace-element composition and U–Pb dating analyses, the laser ablation inductively coupled plasma mass spectrometry (LA-ICP-MS) technique was employed at the Institute of Geomechanics within the Chinese Academy of Geological Sciences. LA-ICP-MS testing utilized a GeoLas HD excimer laser ablation system operating at a 193 nm wavelength (manufactured by Coherent in Santa Clara, CA, USA), coupled with an Agilent7900 four-stage rod mass spectrometer. Carrier gases used during testing included Ar and He. The laser had a pulse rate of 5 Hz and a spot size diameter measuring 44 μm. The energy density applied during testing reached 3 J/cm^2.

The external calibration standards included NIST SRM610 and 612 glass reference materials for element content, the Ontario and the T3 reference materials for U–Pb dating. Data analysis was performed using ICPMSDataCal 11.8 software.

4. Results

4.1. Visual Appearance and Gemological Properties

The gemological properties of the two titanite samples are shown in Table 1. The results show that MA-1 and MA-2 have similar gemological properties. MA-1 is yellow with a good transparency. MA-2 is also yellow, while it is translucent for its dark inclusions and surface damage. The refractive index (RI) of the two titanites is beyond the range of the refractometer (>1.78). The specific gravity (SG) values of MA-1 and MA-2 fall in the range of 3.52~ 3.54. The two titanite samples are inert to both short and long-wave UV radiation.

The microscopic observation showed the original crystal growth characteristics and some inclusions (Figure 4). A crystal edge double shadow can be observed, which is associated with the samples' high birefringence (0.100~0.135).

Table 1. Gemological properties of titanite from Morocco.

Properties	Data	
	MA-1	MA-2
Color	Yellow	Yellow
Diaphaneity	Transparent	Translucent
Luster	Greasy	Weak greasy
RI	>1.78	>1.78
SG	3.52	3.54
Fluorescence reaction	Inert	Inert
Chelsea color filter	Unchanged	Unchanged

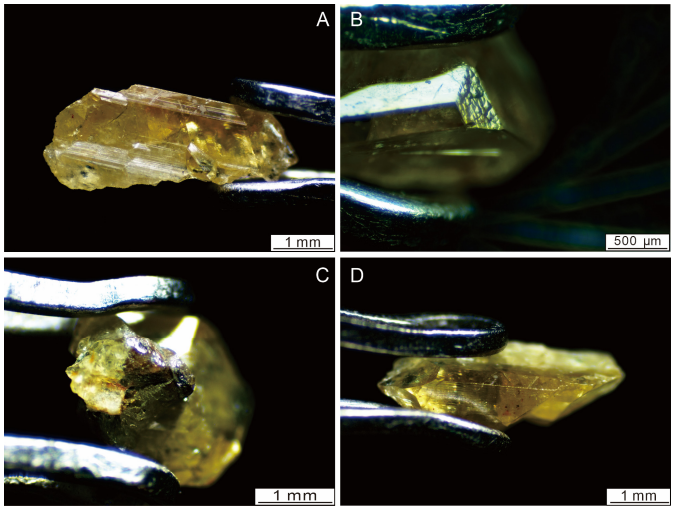

Figure 4. The micrographs of titanite samples MA-1 (**A**,**B**) and MA-2 (**C**,**D**). (**A**) stepped crystal patterns; (**B**) growth mounds; (**C**) solid inclusion; (**D**) longitudinal striations.

The titanite samples exhibit a conchoidal fracture with a greasy luster after smashing. The MA-1 had crystal plane steps (Figure 4A) along the b-axis. The crystal surface of MA-1 raised growth mounds, which were perpendicular to the b-axis (Figure 4B). A brown solid inclusion was found in the tail of the MA-2 (Figure 4C), speculating that it may be rutile. The longitudinal striations can be observed on the surface of titanite parallel to the b-axis (Figure 4D). Because the hardness of the titanite was relatively low (only five), scratches made by the forceps were observed on the surface.

4.2. Spectral Characteristics

The first-order phonon spectra of titanite in the phase $P2_1/a$ are described by the optically active representations: Γ_{optic} = 24 A_g + 2 4B_g + 23 A_u + 22 B_u (A_g and B_g are Raman active, and A_u and B_u IR active) [33,34]. Group theory predicts 48 Raman and 45 infrared active vibration modes in titanite [35,36].

4.2.1. Fourier Transform Infrared Spectrum

The FTIR spectra (Figure 5A) and deconvolution–Gaussian curve fitting spectra (Figure 5B) of MA-1 and MA-2 are practically identical to the corresponding published data. The infrared spectra of titanite samples in the range of 400~4000 cm^{-1} were relatively similar. The characteristic bands of the samples were distributed at 431, 470, 501, 563, 692, 873, 900, and 3475 cm^{-1}. The deconvoluted infrared spectrum displays additional bands at 532, 590, 634, 809, 848, and 925 cm^{-1} in comparison to the original infrared spectra (Table 2).

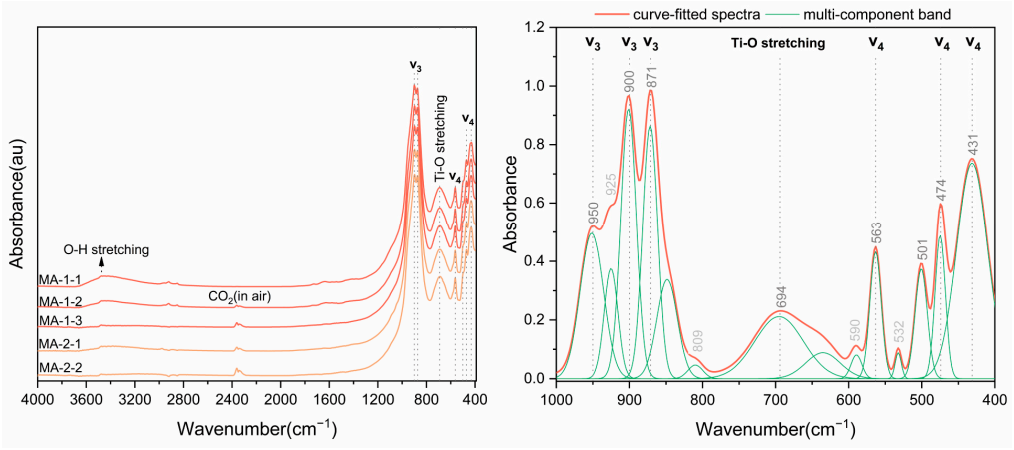

Figure 5. (**A**) FTIR spectra of titanites (MA-1, MA-2) were collected by the transmission method within the 400–4000 cm^{-1} frequency range; (**B**) Infrared spectrum of MA-1 after deconvolution and Gaussian curve fitting in the range of 400–1000 cm^{-1}, exhibiting more bands than the original spectrum.

As seen from the infrared spectra, the ν_3 anti-symmetric stretching mode of SiO_4 groups is split into three components with frequencies at 950, 900, and 873 cm^{-1}, being very close to the literature data [37–40]. Triple splitting is also observed for the ν_4 anti-symmetric bending mode (563, 470, and 431 cm^{-1}), compared to the two components of the ν_4 anti-symmetric bending mode mentioned in the literature [40,41]. The weak band at 501 cm^{-1} is probably related to the Si-O bending. The broad band at 692 cm^{-1} is probably due to the vibrations of the present TiO_6 octahedra in the structure of titanite [39,40]. The intensity of the Ti-O band in the natural titanite samples was found to be correlated with both the Ti content and the level of crystal crystallization [8,34,38,39,41]. The band near 3475 cm^{-1} is mainly due to OH stretching at the O1 site [37,42–44]. The low-temperature IR results of the crystal B20323 also show that the absorption near 3486 cm^{-1} may consist of more than one OH vibration [43]. Four infrared spectra exhibited a weak band at 2362 cm^{-1}, which can be assigned to the CO_2 in air.

Table 2. The bands of titanite in infrared spectra and their deconvolution, with attribution of these bands.

Infrared Bands (cm^{-1})		Assignment [37,39–41]
Original	**Deconvolution**	
431	431	ν_4 anti-symmetric, bending Si-O
470	474	ν_4 anti-symmetric, bending Si-O
501	501	Si-O bending
	532	Si-O bending
563	563	ν_4 anti-symmetric, bending Si-O
	590	Si-O bending
	634	Ti-O stretching
692	694	Ti-O stretching
	809	Si-O stretching
	848	Si-O stretching
873	871	ν_3 anti-symmetric, stretching Si-O
900	900	ν_3 anti-symmetric, stretching Si-O
	925	Si-O stretching
	950	ν_3 anti-symmetric, stretching Si-O
3475		OH stretching

For bands observed at 532, 590, 634, 809, 848, and 925 cm^{-1} following deconvolution, their assignment can be determined based on the available literature [39–41]. The 532 and 590 cm^{-1} bands are due to Si-O bending vibrations of SiO_4 tetrahedra, and the band

at 594 cm^{-1} is due to Ti-O stretching from TiO_6 octahedra. The 809, 848, and 925 cm^{-1} bands are assigned to the Si-O stretching vibrations of SiO_4 tetrahedra. The band of Ca-O vibration is probably below 500 cm^{-1}. Some deviations from the standard results may be related to the substitution of small amounts of Th, Nb, and Ce in place of Ca and Ti [41].

4.2.2. Raman Spectrum

The Raman spectra of titanite samples collected from various orientations within the 400~1200 cm^{-1} range are depicted in Figure 6. The Raman spectra of titanite exhibited nearly 10 bands in this experiment (Table 3), which can be attributed to its low symmetry [9]. The 606 cm^{-1} band of titanite consistently exhibited a narrow half-width and strong intensity across all samples, indicating a high level of conformity with the reference material from the RRUFF database and published literature. Upon comparing the Raman spectra of titanite samples sourced from various regions, it was observed that they exhibited similar bands with slight variations in intensity [31]. However, these findings suggest that relying solely on Raman spectra may not provide conclusive information regarding their origin.

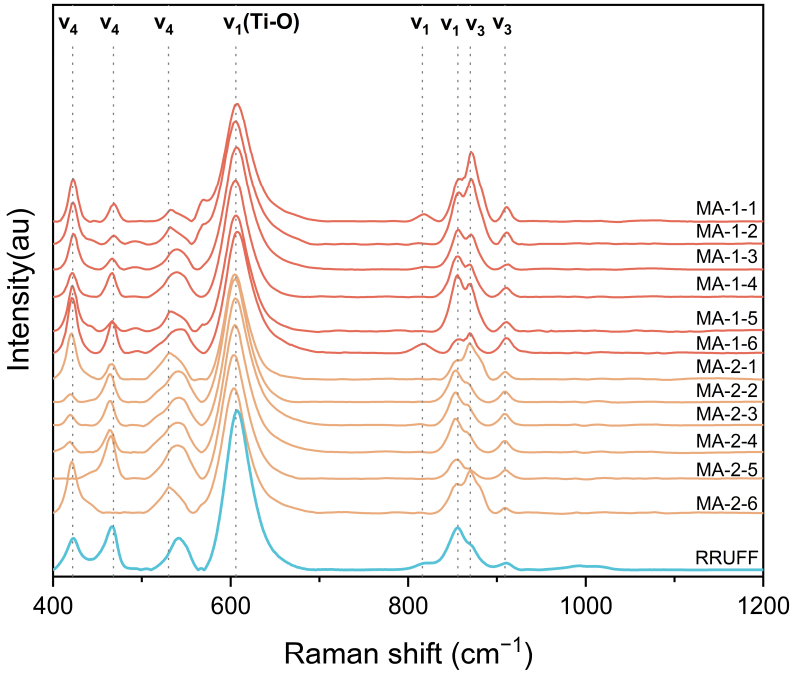

Figure 6. The representative Raman spectra of MA-1 and MA-2 were obtained in the direction perpendicular to the b-axis.

Table 3. The bands of titanite in Raman spectra and their assignment.

Raman Bands(cm^{-1})		Assignment [9,40,45]
MA-1	**MA-2**	
422	420	ν_4 anti-symmetric, bending, deformation Si-O-Si
466	465	ν_4 anti-symmetric, bending, deformation Si-O-Si
531	529	ν_4 anti-symmetric, bending, deformation Si-O-Si
540	540	ν_4 anti-symmetric, bending, deformation Si-O-Si
606	606	Stretching Ti-O in $[SiO_6]^{8-}$ octahedron
816		ν_1 symmetric, stretching Si-O
855	853	ν_1 symmetric, stretching Si-O
870	870	ν_3 anti-symmetric, stretching Si-O
911	909	ν_3 anti-symmetric, stretching Si-O

Based on previous research [9,33,34,40,45–47], the strongest band in the spectrum of titanite samples, at 606 cm^{-1} is due to stretching vibrations of the Ti–O bond in $[TiO_6]^{8-}$ octahedron. The bands at 422, 465, and 540 cm^{-1} are related to anti-symmetric bending vibrations of the Si–O–Si bond (ν_4). The strong band at 853 cm^{-1} is due to fully symmetric stretching vibrations of the Si–O bond (ν_1). The bands at 911 and 870 cm^{-1} originating from anti-symmetric stretching vibrations of the Si–O bond (ν_3) are also characteristic features of the spectrum. In the cited papers, the bands in the range below 420 cm^{-1} are connected with rotations and translations of the whole structural units [9,48].

The Raman spectra obtained from titanite samples exhibited similarities; however, slight variations in intensity and shifts were observed. Although both titanite samples displayed bands at identical positions, their intensities differed. The Raman spectra of each titanite sample obtained from different directions are not the same, especially at 466, 531, 855, and 870 cm^{-1}, which could potentially be attributed to crystal anisotropy.

4.3. Major Elements

Table A1 reports the composition of the major elements, expressed as oxides, and the cations are reported in atoms per formula (apfu). The major element composition of both MA-1 and MA-2 exhibits similarities. Notably, both samples demonstrate a significant enrichment in the V (0.009~0.015 apfu), Al (0.031~0.052 apfu), and Fe (0.016~0.029 apfu). Because Al, Fe, and V substitute for Ti in the octahedral site, titanites show a negative correlation between Al, Fe, V, and Ti (Figure 7). This is consistent with substitutions such as (Al, Fe^{3+}) + (F, OH) ↔ Ti + O [4].

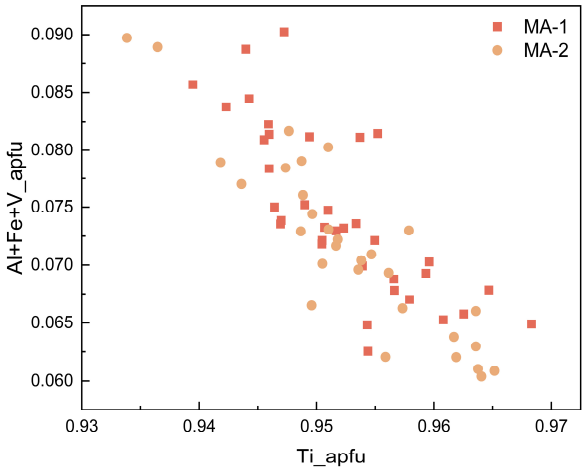

Figure 7. Selected binary plots showing the compositional variations of two titanite samples: plots of Ti versus Fe + Al + V; apfu = atoms per formula.

The formula of MA-1 and MA-2 are $(Ca_{0.981}Na_{0,001})_{0.982}(Ti_{0.952}Al_{0.041}Fe_{0.021}V_{0.013})_{1.027}SiO_5$ and $(Ca_{0.977}Na_{0,001})_{0.978}(Ti_{0.950}Al_{0.039}Fe_{0.020}V_{0.012})_{1.021}SiO_5$.

4.4. Trace Elements

The trace elements of the titanites analyzed by LA-ICP-MS are presented in Tables A2 and A3. It showed that titanite contained a variety of trace elements, especially rare earth elements (REEs). The ∑REE contents of the Moroccan titanites (MA-1, MA-2) are 802~4088 ppm and 933~3077 ppm. And the average values are 1740 ppm and 2100 ppm. The Th and U concentrations of MA-1 are 12.2~422 ppm and 3.99~109 ppm. The Th and U concentrations of MA-2 are 29.4~337 ppm and 6.96~66.7 ppm. The ratios Th/U of the two samples are 0.28~13.61 and 1.04~15.4. MA-1 and MA-2 have high concentrations in Nb with 63.9~2063 ppm and 144~679 ppm, the average values were 425 ppm and 474 ppm. Studying the dispersion patterns of rare earth elements (REEs) can serve as an extremely

useful method for identifying the characteristics and sources of minerals and rocks. The REE diagrams, when normalized to chondrite, exhibited comparable characteristics in the two titanite samples (Figure 8). MA-1 and MA-2 were slightly enriched in light rare earth elements (LREEs) and were depleted in heavy rare earth elements (HREEs).

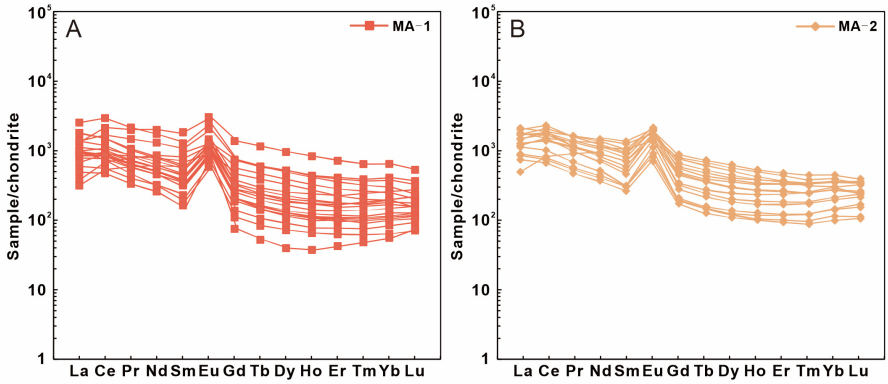

Figure 8. REE patterns of titanites from the Central High Atlas region. Data were normalized to chondrite values obtained from Sun and McDonough (1989) [49].

Furthermore, the δEu $((Eu/\sqrt{(Sm*Gd)})_{titanite}/(Eu/\sqrt{(Sm*Gd)})_{chondrite})$ and δCe $((Ce/\sqrt{(La*Pr)})_{titanite}/(Ce/\sqrt{(La*Pr)})_{chondrite})$ of titanites show pronounced positive anomalies. The values of δEu of MA-1 and MA-2 were 1.56~7.79 and 1.53~4.52. The values of δCe were 1.08~1.33 and 1.10~1.28.

4.5. Titanite U–Pb Ages

The backscattered electron images of the titanite samples showed that most of them are grey-white without cracks (Figure 9). It showed that the internal structure of the titanites was uniform, without component zonation and mineral inclusions. Several sections were analyzed using LA-ICP-MS to obtain approximately 16~20 spots for each titanite sample.

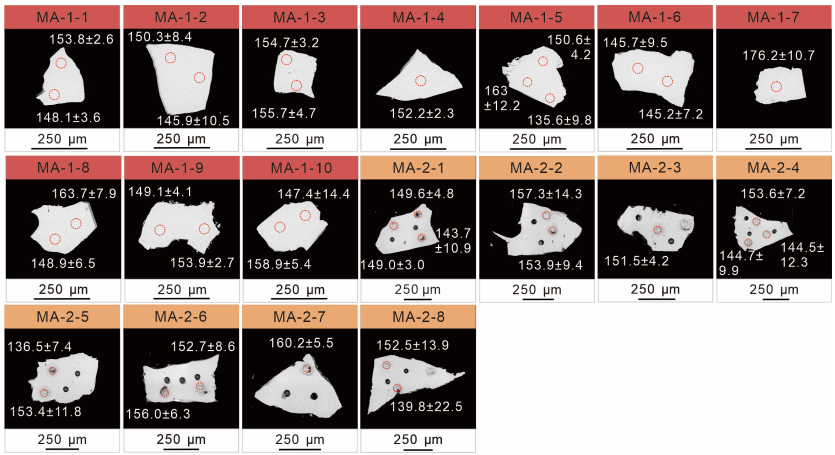

Figure 9. Backscattered electron images of the titanite samples. The red circles represent the analyzed spots.

The LA-ICP-MS analysis yielded Table A4, which presents the titanite U–Pb dating results with uncertainties reported at the 1σ level. The ages of titanite with common Pb were determined by taking into account the weighted mean of the ^{207}Pb-corrected ages and anchoring them through common Pb to the Tera–Wasserburg (TW) Concordia intercept age. The ^{238}U/^{206}Pb and ^{207}Pb/^{206}Pb ratios of MA-1 yields a lower intercept age of 152.6 ± 2.2 Ma (1s, Figure 10A). The ^{207}Pb-corrected weighted average ^{206}Pb/^{238}U age

of MA-1 is 152.3 ± 2.0 Ma (1s, Figure 10B). The $^{238}U/^{206}Pb$ and $^{207}Pb/^{206}Pb$ ratios of MA-2 yield a lower intercept age of 151.4 ± 5.3 Ma (1s, Figure 10C). The ^{207}Pb-corrected weighted average $^{206}Pb/^{238}U$ age is 150.7 ± 3.2 Ma (1s, Figure 10D). The weighted age within error is consistent with its lower intercept age. The results show that two titanites were formed in the late Jurassic.

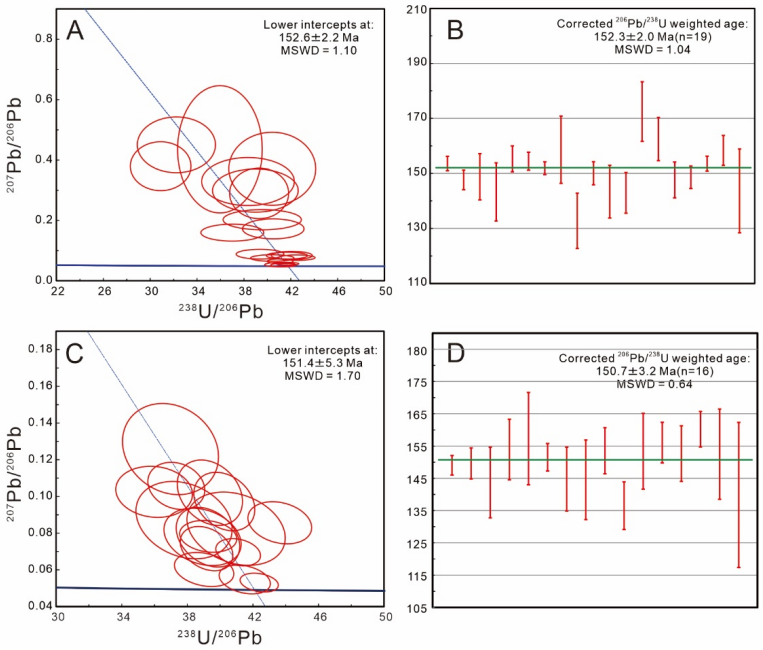

Figure 10. Titanite U–Pb ages by LA-ICP-MS: the Tera–Wasserburg diagram of MA-1 (**A**) and MA-2 (**C**); the weighted average $^{206}Pb/^{238}U$ age plot of MA-1 (**B**) and MA-2 (**D**).

5. Discussion

5.1. Structural State and Radiation Damage

Radiation resulting from naturally occurring impurities (such as U and Th) induces structural damage and amorphization in titanite, which is evident through a significant decrease in band intensity and a broadening of the overall spectral lines in the Raman and infrared spectra of titanite [8,41,50,51]. And frequency shifts of Raman spectra can also be proven. For Raman spectra, the radiation damage causes the band of Ti-O stretching vibration to shift to high frequency (the characteristic bands at 606 and 533 cm^{-1} move to 646 and 544 cm^{-1}, respectively), which is mainly caused by the transformation of the [TiO_6] group to a [TiO_5] group [34]. For the infrared spectrum, the radiation damage to the titanite increased the full width at half maximum of the Si-O stretching vibration band and decreased the intensity of the Ti-O stretching vibration band [34,41]. In this instance, the loss of radiogenic Pb can result in a non-concordant U–Pb age dataset. To thoroughly evaluate the structural condition of titanite, we conducted an analysis on Morocco titanites using parameters derived from infrared and Raman spectra, as well as the α flux Dα (α-decays/g).

The α flux, determined through the analysis of U and Th concentrations, along with the U–Pb age of the samples, indicates the quantity of α decay occurrences per gram. This measurement can be utilized to further assess the radiative intensity since the point at which the U–Pb system reached closure [52,53]. The results of the Dα are shown in Table A4. The α flux of MA-1 was between 0.37 and 6.57 × 10^{16} α-decays/g, with an average of 2.17 × 10^{16} α-decays/g. The α flux of MA-2 was between 0.92 and 5.18 × 10^{16} α-decays/g, with an average of 2.86 × 10^{16} α-decays/g.

The studied titanites show that when Dα was 2.6 × 10^{18} α-decays/g, the titanites were basically in a completely amorphous state, and the p (amorphous fraction) of the

crystals was 1 [50,53], which represents the proportion of volume that has been amorphized compared to the overall volume of the crystal. It should be noted that Dα reflects the total radiation dose received by the samples, while p describes the current radiation damage degree of the samples. The radiation damage results given by them may not be completely consistent. The amorphous fraction is calculated as: p = 1-exp (-Ba Dα), Ba = 2.7(3) × 10^{-19} g [52,54]. The calculation results showed that the amorphous fraction values of titanites in this paper are close to zero, which indicates that the degree of radiational damage in titanites is low.

The FTIR and Raman spectra of all titanite samples have little obvious difference, which may require further study to confirm the effect. Especially, the bands of Raman spectra have a small full width at half maximum, with rich details, indicating that the titanites were less damaged by radiation and the crystal structures were relatively intact. The spectral results support the conclusions of the α flux Dα.

5.2. Formation Conditions and Origin of the Titanite from Morocco

Revealing the diverse sources of titanites is achievable through analyses of their texture and geochemical characteristics [1]. According to previous studies [3,4,10,13,55–63], elements can distinguish magmatic- and hydrothermal-derived titanites (Figure 11). In general, V is enriched in hydrothermal titanite. Hydrothermal titanite has high Nb/Ta ratios (up to 55), low ∑REE contents (up to 15,000 ppm), and low Th/U ratios (<1), while magmatic titanite has low Nb/Ta ratios (4~25), high ∑REE contents (up to 34,000 ppm), and high Th/U ratios (>1). It should be noted that some hydrothermal titanites in Skarn were rich in Th and U and the Th/U ratios were also high (1.3~17.2) in previous studies [64,65], which implies that the element that forms the complex with REEs in the fluid is mainly F, rather than other volatiles such as Cl [66]. The occurrence of fluorapatite associated with titanite in Central High Atlas, Morocco, also supports this interpretation [67–69].

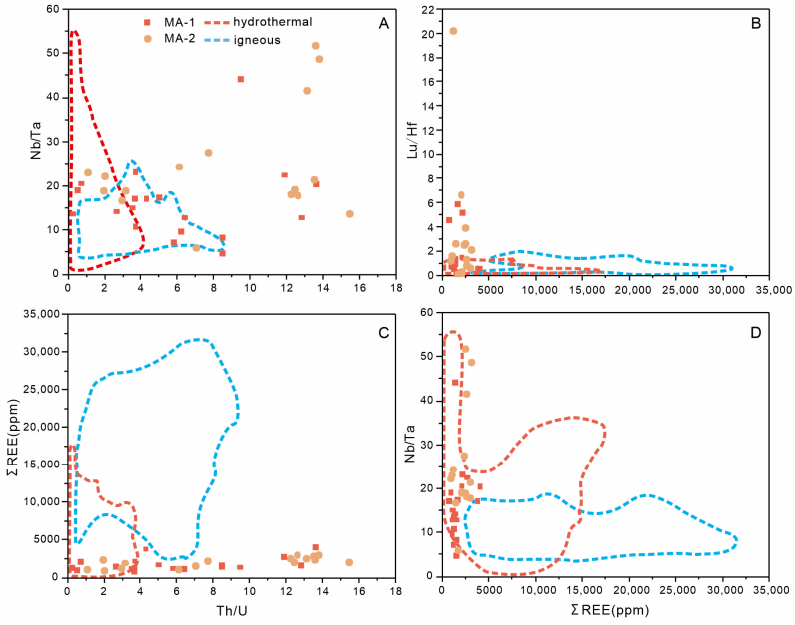

Figure 11. Scatter diagrams of trace elements of titanites.

The ∑REE contents of MA-1 and MA-2 are relatively low (802~4088 ppm). The Nb/Ta ratios are high (5~52). The Th/U ratios exhibit a wide range of variability, spanning from 0.28 to 15.4. MA-1 and MA-2 present enrichment in LREE with positive Eu and Ce anomalies, which are similar to the REEs pattern previously studied in Skarn (Figure 12A). In addition, these samples do not show zoned structure in the Backscattered electron images,

with a simple composition. It could be regarded as the product of a single hydrothermal crystallization. These results match with hydrothermal titanite.

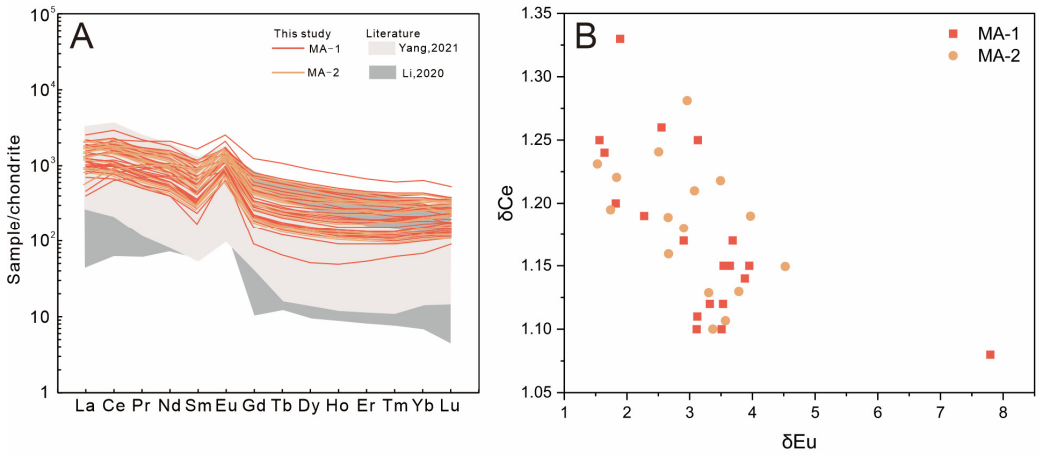

Figure 12. (**A**) Chondrite-normalized rare earth element patterns with reference [64,65] and (**B**) scatter diagram of δEu-δCe.

The oxygen fugacity of the ore-forming fluids can be assessed by analyzing the δ Eu and δ Ce values in titanites [70,71]. In Morocco titanite crystals, there is a negative correlation between δEu and δCe. (Figure 12B). This suggests that variations in the concentration of these elements were primarily influenced by changes in oxidation state [60]. Previous studies on hydrothermal titanite have indicated that those with positive Eu anomalies or high δ Ce values typically indicate a lower oxygen fugacity during their formation [72]. In a reducing environment, Eu undergoes a valence state change from $Eu3^{+}$ to Eu^{2+}, which has a similar ionic radius and valence state as Ca^{2+}. Consequently, Eu^{2+} can easily substitute for Ca^{2+} within the titanite crystal structure, resulting in fractionation from other REE^{3+} and leading to positive Eu anomalies [73]. Titanites from Morocco exhibit significant positive Eu anomalies (δEu: 1.53~7.79) and weak positive Ce anomalies (δCe: 1.08~1.33), suggesting a relatively lower oxygen fugacity within the ore-forming fluids [61,73,74].

To sum up, titanite in Central High Atlas, Morocco, is formed in a hydrothermal environment with a low oxygen fugacity.

5.3. Moroccan Titanite U–Pb Geochronology

The $^{238}U/^{206}Pb$ and $^{207}Pb/^{206}Pb$ ratios of MA-1 and MA-2 yield a lower intercept age of 152.6 ± 2.2 and 151.4 ± 5.3 Ma (1s). The weighted average $^{206}Pb/^{238}U$ age is 152.3 ± 2.0 and 150.7 ± 3.2 Ma (1s), which within error is consistent with its lower intercept age, indicating that these U–Pb data have a high reliability. This consistent U–Pb dating age of the two titanites implies that there has been a negligible depletion of radiogenic Pb in the U–Pb system since the formation of the titanite.

The orogenic development of Morocco's High Atlas intracontinental belt throughout the Mesozoic–Cenozoic involved three primary instances of magmatic activities [31,75]. The initial occurrence of magmatic activity took place during the Late Triassic when there was a widespread emission of tholeiitic basaltic lavas, which were part of the Central Atlantic Magmatic Province [76–78]. Following this, a geographically limited but petrologically diverse transitional to alkaline magmatism occurred in the Central High Atlas region during the late Jurassic to early Cretaceous [29,79]. The last magmatic event was displayed by the Eocene Tamazert alkaline complex located within the Central High Atlas belt [80–82].

During the second period, the transitional to alkaline magmatic activity of the Central High Atlas occurred between 165 and 125 Ma, possibly with two peaks [28,31,83,84]. Based on published data on igneous rocks from the Central High Atlas, Bensalah et al. defined two major peaks at about 152 Ma and about 118 Ma [25]. The U–Pb ages of the two titanites

were 151–152 Ma and showed a similar distribution of rare earth elements, which indicated that the ore-forming fluids were from the same magma hydrothermal in the late Jurassic. The results of U–Pb dating are consistent with the peak of 152 Ma.

In addition, the technique of isotope dilution thermal ionization mass spectrometry (ID-TIMS) exhibits a higher level of analytical precision (0.1%) in comparison to the LA-ICP-MS technique [85]. To validate the absolute accuracy of the LA-ICP-MS age and assess its potential as a reference material, it is necessary to employ the ID-TIMS technique for further investigation into the dispersed fragments.

6. Conclusions

We have investigated the gemological and chemical characteristics of titanite samples from Morocco and analyzed their infrared spectra, Raman spectra, SEM-EDS, U–Pb geochronology, and elemental compositions. The two titanite samples are yellow, transparent-translucent with a greasy luster. The gemological properties and spectral characteristics of the titanite samples are similar to previous studies. The two titanites are rich in V, consisting of a low total REE content, high Nb/Ta ratios, and a relatively variable range of Th/U ratios with positive Eu and Ce anomalies, forming in a hydrothermal environment with a low oxygen fugacity. The titanite samples have almost no radiational damage, and their U–Pb data have a high reliability. The titanite obtained from the High Atlas area in Morocco displays encouraging attributes that make it a prospective reference material for LA-ICP-MS U–Pb dating. Nevertheless, further experimentation is necessary to verify its appropriateness.

Author Contributions: Writing—original draft, Y.Y.; writing—review and editing, Y.Y., Y.Z., Z.M. and B.X.; visualization, Y.Y. and J.G.; software, Y.Y. and P.Y.; supervision, Z.M. and B.X.; methodology, Z.M., Y.Z., B.X., J.G. and P.Y.; funding acquisition, Z.M., Y.Z. and B.X.; investigation, J.G. and P.Y. All authors have read and agreed to the published version of the manuscript.

Funding: This research was funded by the National Key R&D Program of China (2023YFF0804200), National Natural Science Foundation of China (42222304, 42073038, 41803045, 42202084), Young Talent Support Project of CAST, the Fundamental Research Funds for the Central Universities (Grant No. 265QZ2021012), and IGCP-662.

Data Availability Statement: The data presented in this study are available within the article.

Acknowledgments: We thank the editor and reviewers for their constructive comments which helped in improving our paper. This is the 23rd contribution of B.X. for the National Mineral Rock and Fossil Specimens Resource Center.

Conflicts of Interest: The authors declare no conflicts of interest.

Appendix A

Table A1. Major element composition (wt.%) and unit formula (apfu) of titanites.

Sample	M1-1	M1-2	M1-3	M1-4	M1-5	M1-6	M1-7	M1-8	M1-9	M1-10	M1-11
Major (wt%)											
Na_2O	0.007	0.010	0.027	0.003	0.017	0.010	0.003	0.003	0.017	0.010	0.010
2SD	0.009	0.028	0.050	0.009	0.047	0.016	0.009	0.009	0.047	0.028	0.028
MgO	0.010	0.007	0.013	0.003	0.013	0.010	b.d.l	0.020	0.010	b.d.l	b.d.l
2SD	0.016	0.019	0.025	0.009	0.038	0.016	-	0.016	0.028	-	-
Al_2O_3	1.080	0.977	0.973	1.127	0.943	1.093	0.987	1.020	1.160	1.273	1.120
2SD	0.312	0.019	0.057	0.041	0.111	0.125	0.094	0.016	0.156	0.084	0.043
SiO_2	30.46	30.55	30.60	30.48	30.71	30.79	30.66	30.74	30.58	30.61	30.62
2SD	0.509	0.447	0.057	0.313	0.368	0.275	0.646	0.134	0.428	0.259	0.180
K_2O	0.007	0.017	0.007	0.017	0.017	0.027	0.003	0.017	0.010	0.010	0.010
2SD	0.019	0.019	0.009	0.009	0.009	0.009	0.009	0.009	0.016	0.016	0
CaO	28.07	28.00	28.04	28.15	28.03	27.95	28.07	28.01	28.02	28.08	28.16
2SD	0.188	0.229	0.074	0.025	0.249	0.082	0.203	0.019	0.136	0.093	0.109
TiO_2	38.92	38.90	38.86	38.65	38.99	38.73	38.78	38.72	38.57	38.38	38.40
2SD	0.596	0.290	0.147	0.296	0.203	0.164	0.538	0.034	0.164	0.034	0.214

Table A1. *Cont.*

Sample	M1-1	M1-2	M1-3	M1-4	M1-5	M1-6	M1-7	M1-8	M1-9	M1-10	M1-11
V_2O_3	0.460	0.497	0.477	0.517	0.473	0.487	0.473	0.490	0.487	0.507	0.560
2SD	0.107	0.068	0.093	0.025	0.057	0.111	0.047	0.028	0.052	0.084	0.028
MnO	0.017	0.030	0.020	0.023	0.010	0.003	0.043	0.033	0.030	0.033	0.020
2SD	0.025	0.016	0.016	0.009	0.028	0.009	0.009	0.009	0.033	0.050	0.016
Fe_2O_3	0.817	0.807	0.877	0.987	0.673	0.730	0.870	0.843	0.963	0.950	1.030
2SD	0.050	0.052	0.066	0.066	0.068	0.130	0.118	0.041	0.288	0.016	0.082
ZrO_2	b.d.l	0.073	b.d.l	b.d.l	0.037	0.027	0.020	b.d.l	0.027	b.d.l	b.d.l
2SD	-	0.052	-	-	0.041	0.062	0.057	-	0.075	-	-
Total	99.85	99.87	99.90	99.96	99.91	99.85	99.90	99.91	99.88	99.84	99.93
Unit formula (apfu)											
Na	0.001	0.001	0.002	0.000	0.001	0.001	0.000	0.000	0.001	0.001	0.001
Mg	0.000	0.000	0.000	0.000	0.001	0.000	-	0.001	0.000	-	-
Al	0.041	0.037	0.037	0.043	0.036	0.042	0.038	0.039	0.045	0.049	0.043
Si	0.996	0.998	1.000	0.996	1.002	1.005	1.001	1.003	0.999	1.000	1.000
K	0.000	0.000	0.000	0.001	0.001	0.001	0.000	0.001	0.000	0.000	0.000
Ca	0.983	0.981	0.981	0.985	0.980	0.977	0.982	0.980	0.981	0.983	0.986
Ti	0.957	0.956	0.955	0.950	0.957	0.951	0.953	0.951	0.948	0.943	0.944
V	0.012	0.013	0.012	0.014	0.012	0.013	0.013	0.013	0.013	0.013	0.015
Mn	0.001	0.001	0.001	0.001	0.000	0.000	0.001	0.001	0.001	0.001	0.001
Fe	0.020	0.020	0.022	0.024	0.017	0.018	0.021	0.021	0.024	0.023	0.025
Zr	-	0.001	-	-	0.001	0.000	0.000	-	0.000	-	-
SUM	3.011	3.009	3.011	3.014	3.008	3.008	3.010	3.010	3.013	3.014	3.015
Major (wt%)											
Na_2O	0.003	0.003	0.023	0.010	0.013	0.010	0.010	0.017	0.007	0.010	0.007
2SD	0.009	0.009	0.034	0.016	0.019	0.016	0.016	0.034	0.019	0.016	0.019
MgO	b.d.l	0.013	0.007	0.013	0.003	b.d.l	0.017	b.d.l	0.007	0.020	0.013
2SD	-	0.019	0.009	0.025	0.009	-	0.009	-	0.009	0	0.009
Al_2O_3	0.947	1.067	0.990	1.073	0.970	0.953	0.830	1.097	0.997	1.303	0.923
2SD	0.062	0.081	0.412	0.052	0.086	0.068	0.085	0.096	0.111	0.105	0.038
SiO_2	30.73	30.85	30.48	30.71	30.79	30.88	30.66	30.61	30.89	30.80	30.64
2SD	0.286	0.152	0.143	0.090	0.189	0.276	0.278	0.315	0.232	0.279	0.329
K_2O	0.013	0.007	0.017	0.013	0.007	0.003	0.013	0.013	0.013	0.013	0.010
2SD	0.025	0.019	0.009	0.025	0.009	0.009	0.019	0.025	0.019	0.025	0.016
CaO	27.99	28.04	28.19	28.06	27.87	27.93	27.93	28.05	28.00	28.03	28.01
2SD	0.128	0.093	0.136	0.093	0.025	0.137	0.173	0.075	0.114	0.065	0.057
TiO_2	39.04	38.56	39.00	38.66	39.02	38.98	39.27	38.74	38.73	38.28	38.92
2SD	0.270	0.395	0.425	0.154	0.365	0.170	0.081	0.270	0.077	0.435	0.395
V_2O_3	0.463	0.447	0.480	0.473	0.497	0.423	0.463	0.490	0.463	0.473	0.497
2SD	0.019	0.137	0.028	0.009	0.090	0.133	0.109	0.016	0.062	0.093	0.118
MnO	0.013	0.023	0.030	0.013	0.020	0.023	0.027	0.013	0.020	0.040	0.023
2SD	0.019	0.034	0.016	0.038	0.043	0.009	0.075	0.019	0.016	0.033	0.025
Fe_2O_3	0.707	0.917	0.733	0.880	0.730	0.757	0.680	0.853	0.813	0.990	0.833
2SD	0.038	0.066	0.050	0.091	0.134	0.068	0.049	0.111	0.106	0.049	0.082
ZrO_2	b.d.l	0.003	0.043	b.d.l	0.027	b.d.l	0.007	0.010	0.040	b.d.l	0.037
2SD	-	0.009	0.074	-	0.075	-	0.019	0.028	0.059	-	0.090
Total	99.91	99.94	99.98	99.91	99.94	99.97	99.90	99.89	99.98	99.95	99.92
Unit formula (apfu)											
Na	0.000	0.000	0.002	0.001	0.001	0.001	0.001	0.001	0.000	0.001	0.000
Mg	-	0.001	0.000	0.000	0.000	-	0.001	-	0.000	0.001	0.000
Al	0.036	0.041	0.038	0.041	0.038	0.036	0.032	0.042	0.038	0.050	0.036
Si	1.003	1.006	0.995	1.003	1.004	1.006	1.001	1.000	1.007	1.005	1.001
K	0.000	0.000	0.001	0.000	0.000	0.000	0.001	0.000	0.001	0.000	0.000
Ca	0.979	0.980	0.986	0.982	0.974	0.975	0.977	0.982	0.978	0.980	0.980
Ti	0.958	0.947	0.958	0.949	0.957	0.956	0.964	0.952	0.950	0.939	0.956
V	0.012	0.012	0.012	0.012	0.013	0.011	0.012	0.013	0.012	0.013	0.013
Mn	0.001	0.001	0.001	0.000	0.000	0.001	0.001	0.001	0.001	0.001	0.001
Fe	0.018	0.023	0.018	0.021	0.018	0.018	0.017	0.021	0.020	0.024	0.021
Zr	-	0.000	0.001	-	0.000	-	0.000	0.000	0.001	-	0.001
SUM	3.007	3.010	3.012	3.011	3.005	3.005	3.005	3.011	3.008	3.013	3.009

NOTE: (1) The major element composition represents the average of three repeated measurements for each analysis point. (2) 2SD = 2 standard deviation. (3) b.d.l. = below detectable level.

Table A2. Trace element abundance, ΣREE, LREE/HREE, Ce anomalies, and Eu anomalies in MA-1 titanite.

		MA-1																			
		1	**2**	**3**	**4**	**5**	**6**	**7**	**8**	**9**	**10**	**11**	**12**	**13**	**14**	**15**	**16**	**17**	**18**	**19**	**Avg.**
Nb	ppm	2063	942	187	63.9	248	348	549	193	186	380	298	441	263	262	324	295	374	518	280	432.43
	1s	36.46	12.42	2.68	1.06	3.56	6.39	9.09	3.05	2.50	5.55	9.69	6.74	3.82	4.24	5.35	3.04	6.52	7.87	3.92	7.05
Ta	ppm	120	46.2	4.24	3.74	14.3	15.0	26.7	20.0	25.9	26.7	35.8	94.0	20.5	24.4	21.5	15.5	27.4	23.0	21.7	30.87
	1s	1.70	0.58	0.09	0.08	0.22	0.27	0.46	0.26	0.38	0.32	1.58	1.09	0.33	0.42	0.32	0.22	0.43	0.33	0.32	0.49
Hf	ppm	20.2	15.6	2.39	0.42	0.77	1.09	3.07	2.97	4.90	3.53	15.7	49.7	18.0	3.93	3.09	2.35	3.39	8.60	4.11	8.63
	1s	0.47	0.37	0.15	0.06	0.08	0.08	0.13	0.13	0.19	0.14	1.09	0.79	0.35	0.18	0.16	0.12	0.16	0.25	0.18	0.27
Y	ppm	879	444	177	83.9	181	245	184	116	129	152	339	449	199	124	112	40.0	98.8	442	273	245.76
	1s	11.69	5.35	1.99	1.06	1.83	3.67	2.20	1.33	1.53	1.71	10.96	4.14	2.76	1.54	1.15	0.52	1.10	6.02	3.53	3.37
La	ppm	306	600	197	141	326	421	428	187	201	266	160	89.6	235	219	217	236	233	325	74.7	255.85
	1s	3.68	7.06	2.14	1.88	3.26	4.98	5.38	2.29	2.73	3.54	2.14	1.21	2.73	2.91	2.59	3.32	2.85	3.72	1.33	3.14
Ce	ppm	1302	1799	584	342	728	927	923	470	513	624	550	419	661	556	513	450	530	1034	327	697.46
	1s	24.92	29.76	9.13	4.75	10.59	12.83	15.90	7.23	5.50	11.04	6.00	5.42	9.09	10.93	7.21	6.22	6.60	15.32	5.92	10.76
Pr	ppm	188	205	67.1	38.1	78.5	101	96.5	53.7	59.6	69.6	79.4	75.1	81.5	61.8	55.5	43.9	60.1	140	56.0	84.73
	1s	2.93	3.15	0.93	0.61	1.16	1.83	1.38	0.86	0.84	1.08	1.42	1.02	1.07	1.15	0.78	0.97	0.86	2.35	0.95	1.33
Nd	ppm	931	815	269	150	289	383	365	213	234	271	379	401	331	242	215	148	240	610	288	356.62
	1s	11.61	11.83	4.01	2.22	4.11	5.15	5.63	3.45	3.32	3.93	9.03	4.94	5.09	4.30	3.46	2.92	3.01	8.60	4.64	5.33
Sm	ppm	233	158	54.3	27.0	55.1	73.1	68.5	41.1	40.5	50.8	98.2	118	67.9	42.9	39.1	18.6	43.3	138	85.7	76.49
	1s	3.18	2.60	1.07	0.67	0.95	1.60	1.36	0.86	0.90	1.30	3.26	2.21	1.20	0.96	0.87	0.63	0.88	2.58	1.44	1.50
Eu	ppm	143	117	51.2	31.4	57.4	68.3	61.1	42.9	47.8	49.5	56.7	60.7	57.7	45.6	41.4	38.7	43.8	95.5	43.3	60.65
	1s	2.08	1.64	0.70	0.65	1.00	1.24	0.92	0.79	0.79	0.87	1.07	0.93	0.81	0.76	0.61	0.67	0.72	1.40	0.79	0.97
Gd	ppm	228	124	46.1	22.6	44.7	61.9	52.2	33.4	33.8	41.0	92.4	119	54.4	33.4	30.9	12.4	33.6	119	76.4	66.29
	1s	2.87	2.02	0.88	0.55	0.80	1.02	0.96	0.79	0.68	0.94	3.26	1.78	1.01	0.70	0.72	0.42	0.83	2.13	1.27	1.24
Tb	ppm	34.9	18.0	7.04	3.17	6.39	8.69	7.09	4.65	4.85	5.67	13.9	17.7	7.95	4.76	4.26	1.58	4.31	17.4	11.5	9.67
	1s	0.48	0.30	0.12	0.08	0.13	0.15	0.13	0.11	0.11	0.11	0.50	0.24	0.15	0.12	0.09	0.06	0.11	0.31	0.20	0.18
Dy	ppm	196	106	38.5	18.4	37.2	51.6	41.4	25.8	27.5	32.5	78.6	99.0	45.3	26.2	24.3	8.1	23.2	106	66.6	55.39
	1s	2.91	1.67	0.71	0.38	0.59	0.81	0.82	0.49	0.57	0.59	2.63	1.39	0.86	0.55	0.48	0.25	0.44	1.72	0.97	0.99
Ho	ppm	37.9	20.0	7.77	3.53	7.83	10.9	8.51	4.97	5.61	6.34	14.6	18.7	8.90	5.14	4.87	1.71	4.51	19.5	12.2	10.71
	1s	0.53	0.30	0.15	0.08	0.14	0.18	0.15	0.10	0.13	0.12	0.50	0.26	0.18	0.10	0.11	0.05	0.10	0.39	0.17	0.20
Er	ppm	95.5	54.9	20.5	10.2	22.4	30.2	23.3	14.0	15.6	18.2	37.2	46.9	23.5	14.6	12.8	5.68	13.5	51.8	29.4	28.44
	1s	1.17	0.92	0.46	0.24	0.46	0.48	0.48	0.34	0.32	0.39	1.26	0.57	0.51	0.37	0.30	0.19	0.31	0.87	0.53	0.54
Tm	ppm	13.2	8.00	3.27	1.55	3.78	5.02	3.54	2.14	2.36	2.78	5.40	6.49	3.46	2.24	2.04	0.99	1.86	7.53	4.10	4.20
	1s	0.21	0.14	0.08	0.06	0.09	0.11	0.11	0.06	0.07	0.07	0.18	0.11	0.10	0.09	0.05	0.04	0.07	0.16	0.11	0.10
Yb	ppm	88.5	56.2	23.2	11.5	27.5	35.8	27.3	15.2	17.5	20.3	33.8	41.0	25.1	15.8	14.2	7.65	13.8	51.7	26.5	29.08
	1s	1.46	0.91	0.55	0.34	0.50	0.63	0.49	0.42	0.40	0.37	1.23	0.74	0.55	0.44	0.34	0.30	0.37	0.82	0.54	0.60
Lu	ppm	10.88	7.50	3.20	1.92	4.53	5.65	4.52	2.43	2.61	3.28	4.06	4.77	3.60	2.63	2.38	1.56	2.16	6.62	3.06	4.07
	1s	0.17	0.16	0.09	0.07	0.10	0.13	0.10	0.07	0.08	0.08	0.11	0.12	0.10	0.07	0.07	0.07	0.06	0.15	0.09	0.10
ΣREE		3808	4088	1373	802	1688	2182	2110	1110	1205	1461	1603	1517	1607	1272	1177	975	1248	2722	1104	1739.64
LREE/HREE		4.41	9.36	8.18	9.99	9.94	9.41	11.57	9.83	9.97	10.22	4.73	3.28	8.33	11.14	11.28	23.52	11.88	6.17	3.80	9.32
δEu		1.89	2.55	3.13	3.88	3.53	3.11	3.12	3.54	3.95	3.32	1.82	1.56	2.90	3.68	3.64	7.79	3.51	2.27	1.64	3.20
δCe		1.33	1.26	1.25	1.14	1.12	1.10	1.11	1.15	1.15	1.12	1.20	1.25	1.17	1.17	1.15	1.08	1.10	1.19	1.24	1.17

Table A3. Trace element abundance, ΣREE, LREE/HREE, Ce anomalies, and Eu anomalies in MA-2 titanite.

		MA-2																
		1	**2**	**3**	**4**	**5**	**6**	**7**	**8**	**9**	**10**	**11**	**12**	**13**	**14**	**15**	**16**	**Avg.**
Nb	ppm	399	272	636	305	144	360	489	679	585	651	672	631	504	289	577	393	474.19
	1sigma	6.90	5.42	13.59	5.13	1.45	6.02	8.53	9.40	8.51	10.67	9.20	8.94	9.84	5.23	9.66	4.35	7.68
Ta	ppm	21.0	14.2	32.9	13.7	5.91	15.6	26.8	38.0	21.3	13.3	16.1	29.2	9.73	17.2	94.8	28.3	24.87
	1sigma	0.39	0.28	0.46	0.28	0.10	0.27	0.69	0.52	0.45	0.26	0.30	0.50	0.17	0.35	1.41	0.47	0.43
Hf	ppm	1.16	0.62	30.8	1.62	0.15	1.34	8.63	12.9	2.49	3.26	5.25	10.7	2.53	1.24	43.9	17.3	8.99
	1sigma	0.08	0.07	0.56	0.12	0.04	0.10	0.30	0.31	0.14	0.19	0.21	0.35	0.15	0.08	1.21	0.42	0.27
Y	ppm	189	170	279	98.6	128	109	473	506	253	350	373	377	328	115	430	276	278.43
	1sigma	2.79	2.79	3.50	1.61	1.67	1.47	9.09	7.91	4.63	3.94	4.08	4.31	3.95	1.43	4.88	3.41	3.84
La	ppm	493	418	296	172	208	197	276	336	395	467	392	398	347	262	115	292	316.39
	1sigma	7.48	5.95	5.18	2.58	2.51	2.77	4.34	3.88	6.22	5.83	6.37	5.12	5.23	3.98	1.91	4.24	4.60
Ce	ppm	1132	909	828	400	475	446	909	1127	1038	1382	1091	1245	1021	609	493	852	872.37
	1sigma	22.73	15.27	10.36	7.43	5.36	7.73	17.18	18.86	25.55	22.94	21.49	24.06	14.64	10.57	6.30	10.40	15.05
Pr	ppm	110	93.3	104	43.8	53.3	50.1	126	152	111	150	129	152	123	64.5	84.0	107	103.40
	1sigma	1.99	1.53	1.77	0.62	0.62	0.94	2.06	1.78	1.80	1.94	1.62	2.17	1.77	1.18	1.16	1.82	1.55
Nd	ppm	389	326	414	170	203	190	603	671	410	578	527	637	495	236	435	433	419.84
	1sigma	5.31	5.88	6.38	2.96	2.83	2.71	11.26	8.73	7.19	8.63	8.04	9.04	7.58	3.85	4.63	6.45	6.34
Sm	ppm	61.2	54.3	82.8	30.8	36.4	35.7	147	160	69.5	110	105	122	93.2	36.5	123	83.1	84.49
	1sigma	1.32	0.96	1.82	0.70	0.74	0.92	2.95	3.31	1.44	2.19	1.88	2.03	1.44	1.01	2.18	1.47	1.65
Eu	ppm	72.7	60.4	66.6	31.4	40.5	36.2	77.2	89.8	70.1	96.0	86.2	92.9	85.8	49.9	61.1	74.8	68.22
	1sigma	1.49	0.99	1.23	0.66	0.47	0.79	1.47	1.53	1.21	1.69	1.50	1.23	1.42	0.96	1.05	1.28	1.19
Gd	ppm	51.3	43.9	70.7	27.4	33.0	30.3	126	140	54.2	89.0	93.5	105	78.0	31.2	121	74.6	73.05
	1sigma	1.27	0.92	1.31	0.82	0.78	0.81	2.68	2.72	1.04	1.50	1.73	1.60	1.45	0.84	1.51	1.40	1.40
Tb	ppm	7.05	6.25	10.3	3.63	4.51	4.18	19.9	21.0	7.90	12.4	13.9	15.2	11.3	4.32	17.8	10.6	10.64
	1sigma	0.16	0.14	0.21	0.10	0.11	0.10	0.50	0.37	0.15	0.22	0.27	0.25	0.22	0.12	0.23	0.19	0.21
Dy	ppm	39.2	35.6	57.9	21.1	26.7	23.7	110	123	47.9	74.9	80.1	87.3	69.4	24.3	102	59.0	61.37
	1sigma	0.85	0.68	0.81	0.47	0.56	0.54	2.25	2.24	0.93	1.18	1.39	1.38	1.16	0.61	1.53	1.13	1.11
Ho	ppm	8.13	7.30	11.5	4.37	5.55	4.52	21.8	23.1	10.1	14.9	16.4	16.8	14.2	5.08	18.5	11.8	12.13
	1sigma	0.17	0.15	0.23	0.12	0.12	0.11	0.44	0.43	0.24	0.26	0.28	0.23	0.24	0.13	0.21	0.23	0.22
Er	ppm	23.1	21.3	32.6	11.8	15.4	12.7	56.5	60.7	29.6	42.2	46.5	44.7	41.6	14.9	47.4	34.1	33.44
	1sigma	0.43	0.41	0.55	0.31	0.31	0.35	1.36	1.10	0.50	0.69	0.82	0.82	0.67	0.34	0.78	0.62	0.63
Tm	ppm	3.53	3.36	4.77	1.71	2.37	1.87	7.44	8.71	4.87	6.40	6.68	6.46	6.34	2.34	6.11	4.79	4.86
	1sigma	0.11	0.09	0.11	0.07	0.08	0.07	0.18	0.19	0.12	0.15	0.14	0.16	0.12	0.08	0.14	0.12	0.12
Yb	ppm	27.5	25.5	35.7	12.8	18.3	14.8	51.5	58.2	38.4	47.1	47.0	45.5	47.1	18.8	39.5	35.2	35.19
	1sigma	0.66	0.64	0.63	0.35	0.45	0.44	1.01	1.27	0.82	0.88	0.91	0.90	0.81	0.52	0.67	0.67	0.73
Lu	ppm	4.56	4.16	5.11	2.04	2.98	2.19	6.64	7.66	6.24	6.79	7.00	6.63	6.67	3.26	4.70	4.85	5.09
	1sigma	0.12	0.10	0.12	0.08	0.10	0.07	0.17	0.19	0.13	0.14	0.14	0.11	0.14	0.10	0.12	0.11	0.12
ΣREE		2422	2008	2020	933	1125	1050	2538	2978	2292	3077	2641	2975	2439	1362	1668	2078	2100.47
LREE/HREE		13.74	12.62	7.84	9.99	9.34	10.14	5.35	5.74	10.51	9.47	7.49	8.08	7.88	12.07	3.67	7.84	8.86
δEu		3.97	3.78	2.66	3.30	3.57	3.37	1.74	1.83	3.49	2.96	2.66	2.50	3.08	4.52	1.53	2.90	2.99
δCe		1.19	1.13	1.16	1.13	1.11	1.10	1.19	1.22	1.22	1.28	1.19	1.24	1.21	1.15	1.23	1.18	1.18

Table A4. LA-ICP-MS dating results.

Sample No.	Pb ppm	Th ppm	U ppm	Measured Isotopic Ratios						^{207}Pb-Corrected Ages (Ma)		Dα (α/g)
				^{207}Pb/^{206}Pb	1sigma	^{207}Pb/^{235}U	1sigma	^{206}Pb/^{238}U	1sigma	^{206}Pb/^{238}U	1sigma	10^{16}
MA-1-01	3.39	279	64.98	0.0523	0.0037	0.1715	0.0131	0.0242	0.0004	153.82	2.60	6.57
MA-1-02	3.41	422	31.00	0.0770	0.0058	0.2475	0.0195	0.0235	0.0006	148.08	3.59	6.56
MA-1-03	0.52	54.6	5.75	0.2028	0.0220	0.5808	0.0735	0.0253	0.0014	150.26	8.44	0.94
MA-1-04	0.19	14.6	4.00	0.3291	0.0525	0.7778	0.0975	0.0261	0.0018	145.93	10.54	0.37
MA-1-05	1.32	114	22.90	0.0758	0.0070	0.2547	0.0241	0.0247	0.0007	155.73	4.69	2.50
MA-1-06	1.83	143	38.76	0.0539	0.0049	0.1770	0.0175	0.0243	0.0005	154.72	3.25	3.65
MA-1-07	2.90	78.5	109	0.0567	0.0029	0.1864	0.0110	0.0240	0.0004	152.19	2.31	6.41
MA-1-08	0.43	27.7	4.46	0.4505	0.0610	1.5010	0.1690	0.0310	0.0021	162.96	12.16	0.55
MA-1-09	0.30	28.4	4.90	0.3713	0.0798	0.8531	0.1348	0.0247	0.0015	135.64	9.79	0.58
MA-1-10	0.94	62.6	23.46	0.0837	0.0074	0.2607	0.0231	0.0240	0.0007	150.57	4.18	1.92
MA-1-11	0.46	46.4	5.46	0.2991	0.0471	0.9016	0.0863	0.0257	0.0016	145.71	9.53	0.83
MA-1-12	0.43	46.0	5.44	0.2900	0.0553	0.7831	0.1058	0.0254	0.0011	145.18	7.21	0.82
MA-1-13	0.72	69.4	5.41	0.3799	0.0534	1.3836	0.1793	0.0324	0.0018	176.21	10.74	1.10
MA-1-14	0.40	29.6	7.99	0.1598	0.0185	0.5415	0.0525	0.0270	0.0013	163.69	7.88	0.75
MA-1-15	0.46	35.4	9.96	0.1723	0.0218	0.4986	0.0498	0.0247	0.0011	148.87	6.49	0.92
MA-1-16	0.60	12.2	23.57	0.0841	0.0089	0.2597	0.0268	0.0238	0.0007	149.09	4.10	1.33
MA-1-17	1.09	12.4	44.33	0.0652	0.0052	0.2149	0.0181	0.0243	0.0004	153.89	2.71	2.37
MA-1-18	1.39	162	13.59	0.0885	0.0106	0.2857	0.0316	0.0254	0.0009	158.92	5.44	2.60
MA-1-19	0.30	25.6	3.99	0.4358	0.1391	0.9514	0.1316	0.0278	0.0018	147.42	14.38	0.50
MA-2-01	2.30	130	66.67	0.0545	0.0039	0.1728	0.0123	0.0236	0.0004	149.03	2.99	4.86
MA-2-02	1.46	107	34.16	0.0698	0.0051	0.2337	0.0184	0.0244	0.0005	149.62	4.83	2.96
MA-2-03	1.24	152	12.20	0.0938	0.0169	0.2777	0.0495	0.0244	0.0012	143.67	10.93	2.39
MA-2-04	0.55	29.4	14.51	0.0841	0.0142	0.2764	0.0408	0.0257	0.0010	153.93	9.37	1.07
MA-2-05	0.69	60.9	10.02	0.1144	0.0142	0.3933	0.0404	0.0278	0.0012	157.29	14.31	1.22
MA-2-06	0.94	34.3	33.01	0.0571	0.0058	0.1822	0.0190	0.0241	0.0006	151.54	4.24	2.05
MA-2-07	1.22	140	11.44	0.0993	0.0124	0.3333	0.0400	0.0249	0.0008	144.74	9.88	2.22
MA-2-08	1.70	199	15.81	0.1118	0.0161	0.3576	0.0459	0.0254	0.0008	144.52	12.34	3.13
MA-2-09	2.40	248	32.40	0.0805	0.0069	0.2750	0.0228	0.0255	0.0007	153.57	7.14	4.53
MA-2-10	2.74	337	24.44	0.0876	0.0085	0.2709	0.0269	0.0229	0.0007	136.50	7.39	5.18
MA-2-11	2.34	260	19.86	0.1084	0.0097	0.3911	0.0355	0.0268	0.0008	153.38	11.76	4.05
MA-2-12	2.10	251	18.64	0.0730	0.0089	0.2522	0.0308	0.0256	0.0007	156.05	6.29	3.88
MA-2-13	2.03	250	18.44	0.0840	0.0143	0.2735	0.0413	0.0255	0.0008	152.66	8.61	3.86
MA-2-14	0.88	62.2	21.13	0.0602	0.0066	0.2129	0.0241	0.0256	0.0008	160.21	5.52	1.78
MA-2-15	0.49	49.0	6.96	0.1050	0.0223	0.3180	0.0569	0.0265	0.0014	152.47	13.98	0.92
MA-2-16	0.96	114	7.43	0.1593	0.0281	0.4696	0.0697	0.0271	0.0014	139.82	22.48	1.72

References

1. Cao, M.J.; Qin, K.Z.; Li, G.M.; Evans, N.J.; Jin, L.Y. LA-(MC)-ICP-MS trace element and Nd isotopic compositions and genesis of polygenetic titanite from the Baogutu reduced porphyry Cu deposit, Western Junggar, NW China. *Ore Geol. Rev.* **2015**, *65*, 940–954. [CrossRef]
2. Frost, B.R.; Chamberlain, K.R.; Schumacher, J.C. Sphene (titanite): Phase relations and role as a geochronometer. *Chem. Geol.* **2001**, *172*, 131–148. [CrossRef]
3. Li, J.W.; Deng, X.D.; Zhou, M.F.; Lin, Y.S.; Zhao, X.F.; Guo, J.L. Laser ablation ICP-MS titanite U-Th-Pb dating of hydrothermal ore deposits: A case study of the Tonglushan Cu-Fe-Au skarn deposit, SE Hubei Province, China. *Chem. Geol.* **2010**, *270*, 56–67. [CrossRef]
4. Xiao, X.; Zhou, T.F.; White, N.C.; Zhang, L.J.; Fan, Y.; Chen, X.F. Multiple generations of titanites and their geochemical characteristics record the magmatic-hydrothermal processes and timing of the Dongguashan porphyry-skarn Cu-Au system, Tongling district, Eastern China. *Miner. Depos.* **2021**, *56*, 363–380. [CrossRef]
5. Laurs, B.M. Sphene from northern Pakistan. *Gems Gemol.* **2010**, *46*, 152–153.
6. Quinn, E.P. Sphene from Afghanistan. *Gems Gemol.* **2006**, *42*, 180–182.
7. Renfro, N. Vanadium-bearing color-change sphene from Pakistan/Afghanistan. *Gems Gemol.* **2011**, *47*, 327.
8. Zhang, M.; Salje, E.K.H.; Bismayer, U.; Unruh, H.G.; Wruck, B.; Schmidt, C. Phase Transition(S) in Titanite Catisio5—An Infrared Spectroscopic, Dielectric Response and heat-capacity study. *Phys. Chem. Miner.* **1995**, *22*, 41–49. [CrossRef]
9. Lodzinski, M.; Wrzalik, R.; Sitarz, M. Micro-Raman spectroscopy studies of some accessory minerals from pegmatites of the Sowie Mts and Strzegom-Sobotka massif, Lower Silesia, Poland. *J. Mol. Struct.* **2005**, *744*, 1017–1026. [CrossRef]
10. Deng, X.D.; Li, J.W.; Zhou, M.F.; Zhao, X.F.; Yan, D.R. In-situ LA-ICPMS trace elements and U-Pb analysis of titanite from the Mesozoic Ruanjiawan W-Cu-Mo skarn deposit, Daye district, China. *Ore Geol. Rev.* **2015**, *65*, 990–1004. [CrossRef]
11. Gao, X.Y.; Zheng, Y.F.; Chen, Y.X.; Guo, J.L. Geochemical and U-Pb age constraints on the occurrence of polygenetic titanites in UHP metagranite in the Dabie orogen. *Lithos* **2012**, *136*, 93–108. [CrossRef]
12. Tiepolo, M.; Oberti, R.; Vannucci, R. Trace-element incorporation in titanite: Constraints from experimentally determined solid/liquid partition coefficients. *Chem. Geol.* **2002**, *191*, 105–119. [CrossRef]
13. Fu, Y.; Sun, X.M.; Hollings, P.; Li, D.F.; Yang, T.J. Geochronology and trace element geochemistry of titanite in the Machangqing Cu-Mo-dominated polymetallic deposit, Yunnan Province, southwest China. *J. Asian Earth Sci.* **2018**, *158*, 398–414. [CrossRef]
14. Kohn, M.J. Titanite Petrochronology. *Rev. Miner. Geochem.* **2017**, *83*, 419–441. [CrossRef]
15. Jiang, P.; Yang, K.F.; Fan, H.R.; Liu, X.; Cai, Y.C.; Yang, Y.H. Titanite-scale insights into multi-stage magma mixing in Early Cretaceous of NW Jiaodong terrane, North China Craton. *Lithos* **2016**, *258*, 197–214. [CrossRef]
16. Chew, D.M.; Petrus, J.A.; Kamber, B.S. U-Pb LA-ICPMS dating using accessory mineral standards with variable common Pb. *Chem. Geol.* **2014**, *363*, 185–199. [CrossRef]
17. Luo, T.; Hu, Z.C.; Zhang, W.; Liu, Y.S.; Zong, K.Q.; Zhou, L.; Zhang, J.F.; Hu, S.H. Water Vapor-Assisted "Universal" Nonmatrix-Matched Analytical Method for the in Situ U-Pb Dating of Zircon, Monazite, Titanite, and Xenotime by Laser Ablation-Inductively Coupled Plasma Mass Spectrometry. *Anal. Chem.* **2018**, *90*, 9016–9024. [CrossRef] [PubMed]
18. Sylvester, P.J. Trends in analytical developments and earth science applications in LA-ICP-MS and LA-MC-ICP-MS for 2004 and 2005. *Geostand. Geoanal. Res.* **2006**, *30*, 197–207. [CrossRef]
19. Domènech, M.; Teixell, A.; Babault, J.; Arboleya, M.L. The inverted Triassic rift of the Marrakech High Atlas: A reappraisal of basin geometries and faulting histories. *Tectonophysics* **2015**, *663*, 177–191. [CrossRef]
20. Laville, E.; Pique, A.; Amrhar, M.; Charroud, M. A restatement of the Mesozoic Atlasic Rifting (Morocco). *J. Afr. Earth Sci.* **2004**, *38*, 145–153. [CrossRef]
21. Stampfli, G.M.; Borel, G.D. A plate tectonic model for the Paleozoic and Mesozoic constrained by dynamic plate boundaries and restored synthetic oceanic isochrons. *Earth Planet. Sc. Lett.* **2002**, *196*, 17–33. [CrossRef]
22. Teixell, A.; Arboleya, M.L.; Julivert, M.; Charroud, M. Tectonic shortening and topography in the central High Atlas (Morocco). *Tectonics* **2003**, *22*, 1051. [CrossRef]
23. Gouiza, M.; Bertotti, G.; Hafid, M.; Cloetingh, S. Kinematic and thermal evolution of the Moroccan rifted continental margin: Doukkala-High Atlas transect. *Tectonics* **2010**, *29*, 1–22. [CrossRef]
24. Ouabid, M.; Raji, O.; Dautria, J.M.; Bodinier, J.L.; Parat, F.; El Messbahi, H.; Garrido, C.J.; Ahechach, Y. Petrological and geochemical constraints on the origin of apatite ores from Mesozoic alkaline intrusive complexes, Central High-Atlas, Morocco. *Ore Geol. Rev.* **2021**, *136*, 104250. [CrossRef]
25. Bensalah, M.K.; Youbi, N.; Mata, J.; Madeira, J.; Martins, L.; Font, E.; Medina, F.; Marzoli, A.; El Hachimi, H.; Bertrand, H.; et al. Reply to Comment on "The Jurassic-Cretaceous basaltic magmatism of the Oued El-Abid syncline (High Atlas, Morocco): Physical volcanology, geochemistry and geodynamic implications" by Andre Michard et al. (2013) [J. Afr. Earth Sci. 88 (December) (2013) 101–105]. *J. Afr. Earth Sci.* **2016**, *118*, 320–323. [CrossRef]
26. de Lamotte, D.F.; Saint Bezar, B.A.; Bracène, R.; Mercier, E. The two main steps of the Atlas building and geodynamics of the western Mediterranean. *Tectonics* **2000**, *19*, 740–761. [CrossRef]
27. Tesón, E.; Teixell, A. Sequence of thrusting and syntectonic sedimentation in the eastern Sub-Atlas thrust belt (Dades and Mgoun valleys, Morocco). *Int. J. Earth Sci.* **2008**, *97*, 103–113. [CrossRef]

28. Michard, A.; Ibouh, H.; Charrière, A. Syncline-topped anticlinal ridges from the High Atlas: A Moroccan conundrum, and inspiring structures from the Syrian Arc, Israel. *Terra Nova* **2011**, *23*, 314–323. [CrossRef]
29. Bensalah, M.K.; Youbi, N.; Mata, J.; Madeira, J.; Martins, L.; El Hachimi, H.; Bertrand, H.; Marzoli, A.; Bellieni, G.; Doblas, M.; et al. The Jurassic-Cretaceous basaltic magmatism of the Oued El-Abid syncline (High Atlas, Morocco): Physical volcanology, geochemistry and geodynamic implications. *J. Afr. Earth Sci.* **2013**, *81*, 60–81. [CrossRef]
30. Rahimi, A.; Saidi, A.; Bouabdelli, M.; Beraaouz, E.H.; Rocci, G. Crystallization and fractionation of the post-liassic intrusive series of Tasraft (central High Atlas, Morocco). *Cr Acad. Sci. Ii A* **1997**, *324*, 197–203.
31. Essaifi, A.; Zayane, R. Petrogenesis and origin of the Upper Jurassic-Lower Cretaceous magmatism in Central High Atlas (Morocco): Major, trace element and isotopic (Sr-Nd) constraints. *J. Afr. Earth Sci.* **2018**, *137*, 229–245. [CrossRef]
32. Saura, E.; Vergés, J.; Martín-Martín, J.D.; Mesager, G.; Moragas, M.; Razin, P.; Grélaud, C.; Joussiaume, R.; Malaval, M.; Homke, S.; et al. Syn- to post-rift diapirism and minibasins of the Central High Atlas (Morocco): The changing face of a mountain belt. *J. Geol. Soc. Lond.* **2014**, *171*, 97–105. [CrossRef]
33. Salje, E.; Schmidt, C.; Bismayer, U. Structural Phase-Transition in Titanite, Catisio5—A Raman-Spectroscopic Study. *Phys. Chem. Miner.* **1993**, *19*, 502–506. [CrossRef]
34. Zhang, M.; Salje, E.K.H.; Redfern, S.A.T.; Bismayer, U.; Groat, L.A. Intermediate structures in radiation damaged titanite ($CaTiSiO_5$): A Raman spectroscopic study. *J. Phys-Condens. Mat.* **2013**, *25*, 115402. [CrossRef]
35. Bismayer, U.; Paulmann, C.; Groat, L.; Zhang, M. Local Phenomena in metamict Titanite. *Acta Phys. Pol. A* **2010**, *117*, 74–77. [CrossRef]
36. Mazur, L.; Koszelow, D.; Zajusz, M.; Lapinski, M.; Bik, M.; Zajac, P.; Adamczyk, A.; Rutkowski, P.; Molin, S.; Brylewski, T. Comparison of $Cu_{1.3}Mn_{1.7}O_4$ spinels doped with Ni or Fe and synthesized via wet chemistry and solid-state reaction methods, designed as potential coating materials for metallic interconnects. *J. Eur. Ceram. Soc.* **2023**, *43*, 5557–5574. [CrossRef]
37. Hawthorne, F.C.; Groat, L.A.; Raudsepp, M.; Ball, N.A.; Kimata, M.; Spike, F.D.; Gaba, R.; Halden, N.M.; Lumpkin, G.R.; Ewing, R.C.; et al. Alpha-Decay Damage in Titanite. *Am. Miner.* **1991**, *76*, 370–396.
38. Meyer, H.W.; Zhang, M.; Bismayer, U.; Salje, E.K.H.; Schmidt, C.; Kek, S.; Morgenroth, W.; Bleser, T. Phase transformation of natural titanite: An infrared, Raman spectroscopic, optical birefringence and X-ray diffraction study. *Phase Transit.* **1996**, *59*, 39–60. [CrossRef]
39. Zhang, M.; Salje, E.; Bismayer, U. Structural phase transition near 825 K in titanite: Evidence from infrared spectroscopic observations. *Am. Miner.* **1997**, *82*, 30–35. [CrossRef]
40. Makreski, P.; Jovanovski, G.; Stojanceska, S. Minerals from Macedonia XIII: Vibrational spectra of some commonly appearing nesosilicate minerals. *J. Mol. Struct.* **2005**, *744*, 79–92. [CrossRef]
41. Zhang, M.; Salje, E.K.H.; Bismayer, U.; Groat, L.A.; Malcherek, T. Metamictization and recrystallization of titanite: An infrared spectroscopic study. *Am. Miner.* **2002**, *87*, 882–890. [CrossRef]
42. Hammer, V.M.F.; Beran, A.; Endisch, D.; Rauch, F. OH concentrations in natural titanites determined by FTIR spectroscopy and nuclear reaction analysis. *Eur. J. Mineral.* **1996**, *8*, 281–288. [CrossRef]
43. Zhang, M.; Salje, E.K.H.; Malcherek, T.; Bismayer, U.; Groat, L.A. Dehydration of metamict titanite: An infrared spectroscopic study. *Can. Miner.* **2000**, *38*, 119–130. [CrossRef]
44. Salje, E.K.H.; Zhang, M.; Groat, L.A. Dehydration and recrystallization of radiation-damaged titanite under thermal annealing. *Phase Transit.* **2000**, *71*, 173–187. [CrossRef]
45. Heyns, A.M.; Harden, P.M.; Prinsloo, L.C. Resonance Raman study of the high-pressure phase transition in chromium-doped titanite, $CaTiOSiO_4$. *J. Raman Spectrosc.* **2000**, *31*, 837–841. [CrossRef]
46. Heyns, A.M.; Harden, P.M. The temperature dependence of the Raman spectra of chromium-doped titanite ($CaTiOSiO_4$). *J. Raman Spectrosc.* **2013**, *44*, 1615–1624. [CrossRef]
47. Dumanska-Slowik, M.; Pieczka, A.; Natkaniec-Nowak, L.; Kunecki, P.; Gawel, A.; Heflik, W.; Smolinski, W.; Kozub-Budzyn, G. Mg-enriched erythrite from Bou Azzer, Anti-Atlas Mountains, Morocco: Geochemical and spectroscopic characteristics. *Miner. Petrol.* **2018**, *112*, 381–392. [CrossRef]
48. Beirau, T.; Bismayer, U.; Mihailova, B.; Paulmann, C.; Groat, L. Structural phenomena of metamict titanite: A synchrotron, X-ray diffraction and vibrational spectroscopic study. *Phase Transit.* **2010**, *83*, 694–702. [CrossRef]
49. Sun, S.-S.; McDonough, W.F. Chemical and isotopic systematics of oceanic basalts: Implications for mantle composition and processes. *Geol. Soc. Lond. Spec. Publ.* **1989**, *42*, 313–345. [CrossRef]
50. Beirau, T.; Mihailova, B.; Matveeva, G.; Kolb, U.; Malcherek, T.; Groat, L.A.; Bismayer, U. Structural anisotropy and annealing-induced nanoscale atomic rearrangements in metamict titanite. *Am. Miner.* **2012**, *97*, 1354–1365. [CrossRef]
51. Zhang, M.; Salje, E.K.H.; Farnan, I.; Graeme-Barber, A.; Daniel, P.; Ewing, R.C.; Clark, A.M.; Leroux, H. Metamictization of zircon: Raman spectroscopic study. *J. Phys-Condens. Mat.* **2000**, *12*, 1915–1925. [CrossRef]
52. Murakami, T.; Chakoumakos, B.C.; Ewing, R.C.; Lumpkin, G.R.; Weber, W.J. Alpha-Decay Event Damage in Zircon. *Am. Miner.* **1991**, *76*, 1510–1532.
53. Salje, E.K.H.; Taylor, R.D.; Safarik, D.J.; Lashley, J.C.; Groat, L.A.; Bismayer, U.; Evans, R.J.; Friedman, R. Evidence for direct impact damage in metamict titanite $CaTiSiO_5$. *J. Phys-Condens. Mat.* **2012**, *24*, 052202. [CrossRef] [PubMed]
54. Ríos, S.; Salje, E.K.H.; Zhang, M.; Ewing, R.C. Amorphization in zircon: Evidence for direct impact damage. *J. Phys-Condens. Mat.* **2000**, *12*, 2401–2412. [CrossRef]

55. Duan, Z.; Li, J.W. Zircon and titanite U-Pb dating of the Zhangjiawa iron skarn deposit, Luxi district, North China Craton: Implications for a craton-wide iron skarn mineralization. *Ore Geol. Rev.* **2017**, *89*, 309–323. [CrossRef]
56. Fu, Y.; Sun, X.M.; Zhou, H.Y.; Lin, H.; Yang, T.J. In-situ LA-ICP-MS U-Pb geochronology and trace elements analysis of polygenetic titanite from the giant Beiya gold-polymetallic deposit in Yunnan Province, Southwest China. *Ore Geol. Rev.* **2016**, *77*, 43–56. [CrossRef]
57. Hou, Z.Q.; Xu, B.; Zhang, H.; Zheng, Y.C.; Wang, R.; Liu, Y.; Miao, Z.; Gao, L.; Zhao, Z.; Griffin, W.L.; et al. Refertilized continental root controls the formation of the Mianning-Dechang carbonatite-associated rare-earth-element ore system. *Commun. Earth Environ.* **2023**, *4*, 293. [CrossRef]
58. Hu, H.; Li, J.W.; McFarlane, C.R.M. Hydrothermal titanite from the Chengchao iron skarn deposit: Temporal constraints on iron mineralization, and its potential as a reference material for titanite U-Pb dating. *Miner. Petrol.* **2017**, *111*, 593–608. [CrossRef]
59. Li, J.; Xu, L.L.; Bi, X.W.; Tang, Y.Y.; Sheng, X.Y.; Yu, H.J.; Liu, G.; Ma, R. New titanite U-Pb and molybdenite Re-Os ages for a hydrothermal vein-type Cu deposit in the Lanping Basin, Yunnan, SW China: Constraints on regional metallogeny and implications for exploration. *Miner. Depos.* **2021**, *56*, 441–456. [CrossRef]
60. Pan, L.C.; Hu, R.Z.; Bi, X.W.; Li, C.; Wang, X.S.; Zhu, J.J. Titanite major and trace element compositions as petrogenetic and metallogenic indicators of Mo ore deposits: Examples from four granite plutons in the southern Yidun arc, SW China. *Am. Miner.* **2018**, *103*, 1417–1434. [CrossRef]
61. Song, S.W.; Mao, J.W.; Xie, G.Q.; Chen, L.; Santosh, M.; Chen, G.H.; Rao, J.F.; Ouyang, Y.P. In situ LA-ICP-MS U-Pb geochronology and trace element analysis of hydrothermal titanite from the giant Zhuxi W (Cu) skarn deposit, South China. *Miner. Depos.* **2019**, *54*, 569–590. [CrossRef]
62. Xu, B.; Griffin, W.L.; Xiong, Q.; Hou, Z.Q.; O'Reilly, S.Y.; Guo, Z.; Pearson, N.J.; Gréau, Y.; Yang, Z.M.; Zheng, Y.C. Ultrapotassic rocks and xenoliths from South Tibet: Contrasting styles of interaction between lithospheric mantle and asthenosphere during continental collision. *Geology* **2017**, *45*, 51–54. [CrossRef]
63. Xu, B.; Hou, Z.Q.; Griffin, W.L.; Zheng, Y.C.A.; Wang, T.; Guo, Z.; Hou, J.; Santosh, M.; O'Reilly, S.Y. Cenozoic lithospheric architecture and metallogenesis in Southeastern Tibet. *Earth-Sci Rev.* **2021**, *214*, 103472. [CrossRef]
64. Li, M. Magmatic-Hydrothermal Process of the Pulang Porphyry Copper Deposit, Western Yunnan: Metallogenic Indicator from the Titanite. Master's Thesis, China University of Geosciences, Beijing, China, 2020.
65. Yang, J.-S. Diagenesis and Metallogenesis of the Erdaohe Pb-Zn-Ag Deposit, Inner Mongolia. Ph.D. Thesis, China University of Geosciences, Wuhan, China, 2021.
66. Keppler, H.; Wyllie, P.J. Role of Fluids in Transport and Fractionation of Uranium and Thorium in Magmatic Processes. *Nature* **1990**, *348*, 531–533. [CrossRef]
67. Xu, B.; Hou, Z.Q.; Griffin, W.L.; Yu, J.X.; Long, T.; Zhao, Y.; Wang, T.; Fu, B.; Belousova, E.; O'Reilly, S.Y. Apatite halogens and Sr-O and zircon Hf-O isotopes: Recycled volatiles in Jurassic porphyry ore systems in southern Tibet. *Chem. Geol.* **2022**, *605*, 120924. [CrossRef]
68. Xu, B.; Hou, Z.Q.; Griffin, W.L.; Lu, Y.J.; Belousova, E.; Xu, J.F.; O'Reilly, S.Y. Recycled volatiles determine fertility of porphyry deposits in collisional settings. *Am. Miner.* **2021**, *106*, 656–661. [CrossRef]
69. Yuan, P.; Xu, B.; Wang, Z.; Liu, D. A Study on Apatite from Mesozoic Alkaline Intrusive Complexes, Central High Atlas, Morocco. *Crystals* **2022**, *12*, 461. [CrossRef]
70. Sverjensky, D.A. Europium Redox Equilibria in Aqueous-Solution. *Earth Planet. Sc. Lett.* **1984**, *67*, 70–78. [CrossRef]
71. Xu, L.L.; Bi, X.W.; Hu, R.Z.; Tang, Y.Y.; Wang, X.S.; Xu, Y. LA-ICP-MS mineral chemistry of titanite and the geological implications for exploration of porphyry Cu deposits in the Jinshajiang—Red River alkaline igneous belt, SW China. *Miner. Petrol.* **2015**, *109*, 181–200. [CrossRef]
72. Storey, C.D.; Smith, M.P.; Jeffries, T.E. In situ LA-ICP-MS U-Pb dating of metavolcanics of Norrbotten, Sweden: Records of extended geological histories in complex titanite grains. *Chem. Geol.* **2007**, *240*, 163–181. [CrossRef]
73. Horie, K.; Hidaka, H.; Gauthier-Lafaye, F. Elemental distribution in apatite, titanite and zircon during hydrothermal alteration: Durability of immobilization mineral phases for actinides. *Phys. Chem. Earth* **2008**, *33*, 962–968. [CrossRef]
74. Che, X.D.; Linnen, R.L.; Wang, R.C.; Groat, L.A.; Brand, A.A. Distribution of Trace and Rare Earth Elements in Titanite from Tungsten and Molybdenum Deposits in Yukon and British Columbia, Canada. *Can. Miner.* **2013**, *51*, 415–438. [CrossRef]
75. Marzoli, A.; Bertrand, H.; Knight, K.B.; Cirilli, S.; Buratti, N.; Vérati, C.; Nomade, S.; Renne, P.R.; Youbi, N.; Martini, R.; et al. Synchrony of the Central Atlantic magmatic province and the Triassic-Jurassic boundary climatic and biotic crisis. *Geology* **2004**, *32*, 973–976. [CrossRef]
76. Knight, K.B.; Nomade, S.; Renne, P.R.; Marzoli, A.; Bertrand, H.; Youbi, N. The central Atlantic magmatic province at the Triassic-Jurassic boundary: Paleomagnetic and 40Ar/39Ar evidence from Morocco for brief, episodic volcanism. *Earth Planet. Sci. Lett.* **2004**, *228*, 143–160. [CrossRef]
77. Nomade, S.; Knight, K.B.; Beutel, E.; Renne, P.R.; Verati, C.; Féraud, G.; Marzoli, A.; Youbi, N.; Bertrand, H. Chronology of the Central Atlantic Magmatic Province: Implications for the Central Atlantic rifting processes and the Triassic-Jurassic biotic crisis. *Palaeogeogr. Palaeocl.* **2007**, *244*, 326–344. [CrossRef]
78. Verati, C.; Rapaille, C.; Féraud, G.; Marzoli, A.; Bertrand, H.; Youbi, N. 40Ar/39Ar ages and duration of the Central Atlantic Magmatic Province volcanism in Morocco and Portugal and its relation to the Triassic-Jurassic boundary. *Palaeogeogr. Palaeocl.* **2007**, *244*, 308–325. [CrossRef]

79. Moratti, G.; Benvenuti, M.; Santo, A.P.; Laurenzi, M.A.; Braschi, E.; Tommasini, S. New40Ar-Ar dating of Lower Cretaceous basalts at the southern front of the Central High Atlas, Morocco: Insights on late Mesozoic tectonics, sedimentation and magmatism. *Int. J. Earth Sci.* **2018**, *107*, 2491–2515. [CrossRef]
80. Bouabdellah, M.; Hoernle, K.; Kchit, A.; Duggen, S.; Hauff, F.; Klügel, A.; Lowry, D.; Beaudoin, G. Petrogenesis of the Eocene Tamazert Continental Carbonatites (Central High Atlas, Morocco): Implications for a Common Source for the Tamazert and Canary and Cape Verde Island Carbonatites. *J. Petrol.* **2010**, *51*, 1655–1686. [CrossRef]
81. Marks, M.A.W.; Schilling, J.; Coulson, I.M.; Wenzel, T.; Markl, G. The alkaline-peralkaline Tamazeght complex, High Atlas Mountains, Morocco: Mineral chemistry and petrological constraints for derivation from a compositionally heterogeneous mantle source. *J. Petrol.* **2008**, *49*, 1097–1131. [CrossRef]
82. Salvi, S.; Fontan, F.; Monchoux, P.; Williams-Jones, A.E.; Moine, B. Hydrothermal mobilization of high field strength elements in alkaline igneous systems: Evidence from the Tamazeght complex (Morocco). *Econ. Geol. Bull. Soc.* **2000**, *95*, 559–575. [CrossRef]
83. Haddoumi, H.; Charrière, A.; Mojon, P.O. Stratigraphy and sedimentology of the Jurassic-Cretaceous continental "Redbeds" of the central High Atlas (Morocco): Paleogeographical and geodynamical implications. *Geobios-Lyon.* **2010**, *43*, 433–451. [CrossRef]
84. Allouban, M.; Karaoui, B.; Mahmoudi, A.; Baïdder, L.; Hafid, A.; Goodenough, K.; Eddebbi, A. Petrographic and geochemical study of Jurassic-Cretaceous intrusive massifs (Gabbros-syenites) of the Eastern High Atlas, Morocco (Rich-Talsint axis). *J. Afr. Earth Sci.* **2021**, *184*, 104280. [CrossRef]
85. Schaltegger, U.; Ovtcharova, M.; Gaynor, S.P.; Schoene, B.; Wotzlaw, J.F.; Davies, J.F.H.L.; Farina, F.; Greber, N.D.; Szymanowski, D.; Chelle-Michou, C. Long-term repeatability and interlaboratory reproducibility of high-precision ID-TIMS U-Pb geochronology. *J. Anal. At. Spectrom.* **2021**, *36*, 1466–1477. [CrossRef]